Pergamon

Geochimica et Cosmochimica Acta, Vol. 67, No. 1, pp. 1–15, 2003

0016-7037/03 $22.00 + .00

PII S0016-7037(00)01005-0

Structural evidence for the sorption of Ni(II) atoms on the edges of montmorillonite clay minerals: A polarized X-ray absorption fine structure study

RAINER DÄHN,[1,*] ANDRÉ M. SCHEIDEGGER,[1] ALAIN MANCEAU,[2] MICHEL L. SCHLEGEL,[2,†] BART BAEYENS,[1] MICHAEL H. BRADBURY,[1] and DANIEL CHATEIGNER[3]

[1]Paul Scherrer Institut, Villigen, CH-5232, Switzerland
[2]Environmental Geochemistry Group, LGIT, University J. Fourier and CNRS, BP 53, F-38041 Grenoble Cedex 9, France
[3]Lab. Cristallographie et science des Matériaux, ISMRA F-14050 Caen, France

(*Received December* 12, 2001; *accepted in revised form June* 6, 2002)

Abstract—The nature of surface complexes formed on Ni uptake onto montmorillonite (a dioctahedral smectite) has been investigated over an extended time period by polarized extended X-ray absorption fine structure (P-EXAFS) spectroscopy. Self-supporting films of Ni-sorbed montmorillonite were prepared by contacting Ni and montmorillonite at pH 7.2, high ionic strength (0.3 M $NaClO_4$), and low Ni concentration ($[Ni]_{initial}$ = 19.9 μM) for 14- and 360-d reaction time. The resulting Ni concentration on the clay varied from 4 to 7 μmol/g. Quantitative texture analysis indicates that the montmorillonite particles were well orientated with respect to the plane of the film. The full width at half maximum of the orientation distribution of the c* axes of individual clay platelets about the normal to the film plane was 44.3° (14-d reaction time) and 47.1° (360-d reaction time). These values were used to correct the coordination numbers determined by P-EXAFS for texture effects. Ni K-edge P-EXAFS spectra were recorded at angles between the incident beam and the film normal equal to 10, 35, 55, and 80°. Spectral analysis led to the identification of three nearest cationic subshells containing 2.0 ± 0.5 Al at 3.0 Å and 2.0 ± 0.5 Si at 3.12 Å and 4.0 ± 0.5 Si at 3.26 Å. These distances are characteristic of edge-sharing linkages between Al and Ni octahedra and of corner-sharing linkages between Ni octahedra and Si tetrahedra, as in clay structures. The angular dependence of the Ni-Al and Ni-Si contributions indicates that Ni-Al pairs are oriented parallel to the film plane, whereas Ni-Si pairs are not. The study reveals the formation of Ni inner-sphere mononuclear surface complexes located at the edges of montmorillonite platelets and thus that heavy metals binding to edge sites is a possible sorption mechanism for dioctahedral smectites. Data analysis further suggests that either the number of neighboring Al atoms slightly increases from 1.6 to 2 or that the structural order of the observed surface complexes increases from 0.01 $Å^2$ to 0.005 $Å^2$ with increasing reaction time. On the basis of the low Ni-Al coordination numbers, it appears that over an extended reaction time period of 1 yr the diffusion of Ni atoms in the octahedral layer is not the major uptake mechanism of Ni onto montmorillonite.

1. INTRODUCTION

Sorption, diffusion, and precipitation reactions at the clay minerals–water interface can significantly retard the release of metal ions into the geosphere. For this reason, smectites are used as geochemical barriers in nuclear waste repositories and landfills for hazardous chemicals. To predict the mobility and long-term behavior of heavy metals and radionuclides in smectitic systems, a mechanistic understanding of the chemical processes at the smectite–water interface is of fundamental importance.

The term "smectite" is used to describe a family of expanding 2:1 phyllosilicate minerals that have permanent layer charge between 0.2 and 0.6 charges per half unit cell. The smectite family encompass clay minerals such as montmorillonite, beidellite, nontronite, saponite, and hectorite. Smectites are constructed of a single octahedral sheet sandwiched between two tetrahedral sheets, with the octahedral sheet sharing the apical oxygens of the tetrahedral sheets. Smectites are divided into two subgroups: dioctahedral, when only two of the three octahedral sites per half unit cell are occupied, and trioctahedral, when all three sites are populated (Güven, 1988). In trioctahedral and dioctahedral structures, octahedral cations are surrounded by 6 and 3 octahedral cations, respectively. The octahedral sheet has two different sites, denoted M1 and M2, which have a different hydroxyl configuration (Fig. 1). M1 is the trans octahedron, with OH groups located at opposing corners, and M2 is the cis octahedron, with the OH groups located on the same edge. Only two of the three octahedral positions per half unit cell (2 M2 + M1) are occupied, which can be either the two M2 sites (denoted herein as trans vacant, or tv) or the M1 and one of the two symmetrically independent M2 sites (denoted herein as cis vacant, or cv). Montmorillonite has cv 2:1 layers, and beidellites and nontronites possess tv 2:1 layers (Tsipursky and Drits, 1984). The tv layers have a C2/*m* layer symmetry, whereas cv layers are reduced to a C2 symmetry. The tetrahedral sheets of smectite are composed of a sixfold hexagonal ring of silica tetrahedra. Trioctahedral structures have a flat basal plane, and dioctahedral structures have a corrugated basal plane as a result of the presence of octahedral vacant sites. The Al-Al and Al-Si distances for M1, M2, and cv sites in montmorillonite are listed in Table 1.

Smectites possess a large specific area and a high structural charge (up to 1000 meq/kg), imparting them with important sorptive properties. Layer charge arises from substitutions in either the octahedral sheet (typically from the substitution of low charge species such as Mg^{2+}, Fe^{2+}, or Mn^{2+} for Al^{3+} in

* Author to whom correspondence should be addressed (Rainer.Daehn@psi.ch).
† *Present address:* Commissariat à l'Energie Atomique, CEA-Saclay, DEN/DPC/SCPA/LCRE, BP6, F-91191 Gif-sur-Yvette Cedex, France.

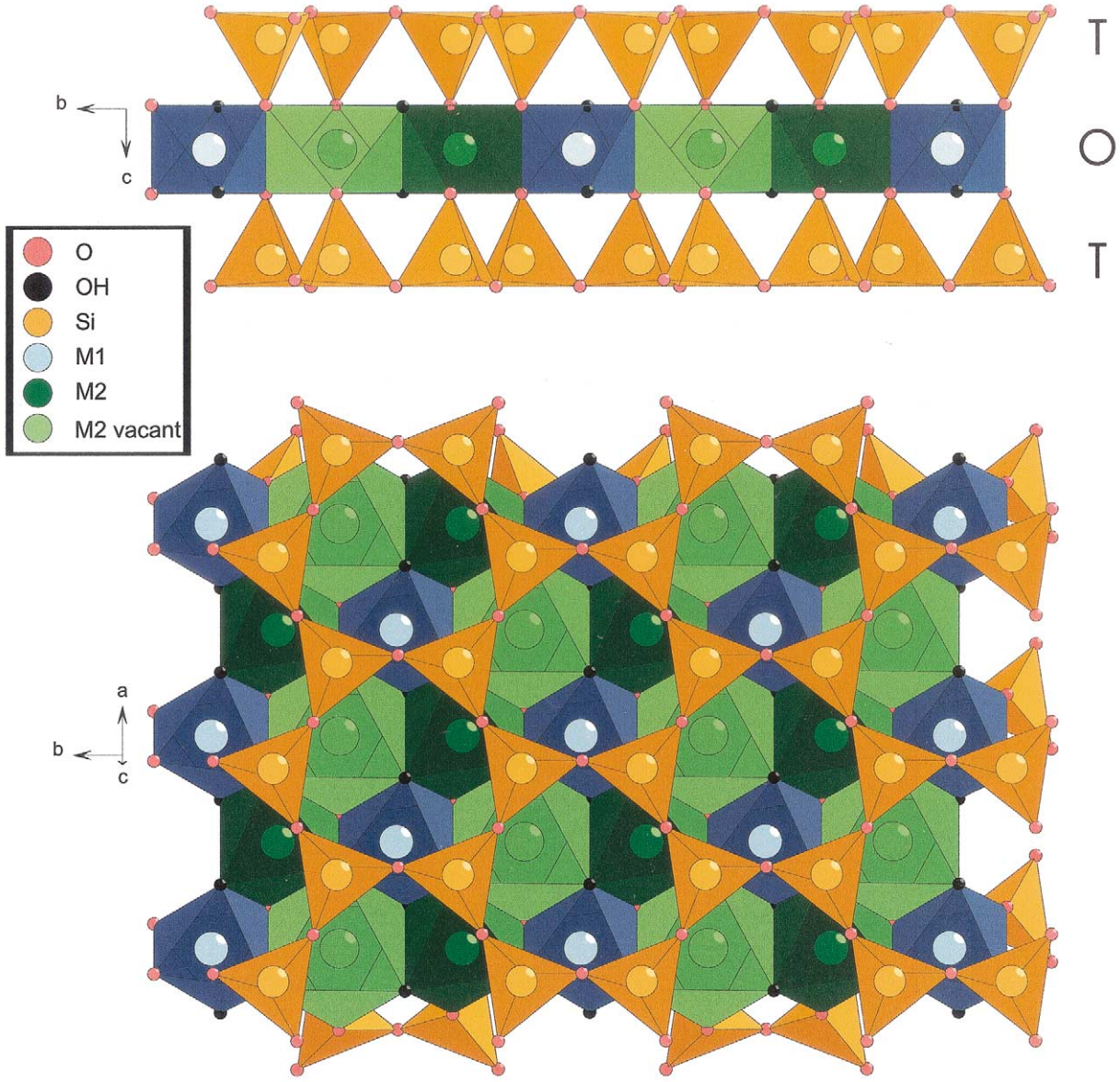

Fig. 1. Structure of montmorillonite after Tsipursky and Drits (1984). The large M2 positions are vacant in montmorillonite.

dioctahedral species) or the tetrahedral sheet (where Al^{3+} or occasionally Fe^{3+} substitutes for Si^{4+}), producing one negative charge for each such substitution. The negative layer charge resulting from isomorphic substitutions is balanced by the sorption of exchangeable cations in interlayer sites (Sposito, 1984). The uptake mechanism of metal ions onto smectites depends on ionic strength, pH, and the type of ion adsorbing. At low pH and low ionic strength, cation exchange is the dominant

Table 1. Al-Al and Al-Si distances in montmorillonite (Tsipursky and Drits, 1984).

	Al-Al		Al-Si1		Al-Si2	
Site	Number of neighbors	Distance (Å)	Number of neighbors	Distance (Å)	Number of neighbors	Distance (Å)
M1	3	2.9–3.1	4	3.16–3.18		
M2	3	2.9–3.1	2	3.15	2	3.23
cv	6	2.9–3.1			4	3.23

process in the interlayer space. In addition to cation exchange, there is a pH-dependent uptake of metals on smectites (Sposito, 1984). In this sorption process, sorbate ions bond to the smectite surface by sharing one or several ligands (generally oxygens) with sorbent cations. At low sorbate cation concentration, specific sorption to surface hydroxyl site (Al-OH, Si-OH) can occur (Schlegel et al., 1999). Metal ions can then directly bond to surface oxygen or hydroxyl groups of the sorbent. With increasing pH or sorbate cation concentration, metal precipitation can occur. When the precipitate contains chemical species derived from both the aqueous solution and dissolution of the sorbent mineral, it is referred to as a coprecipitate (Stumm and Morgan, 1981).

Most uptake studies of metals in clay systems have been performed via a macroscopic approach (batch studies). The focus of many of these studies has been on the determination of distribution coefficients, the use of adsorption isotherms, empirical and semiempirical equations (e.g., Freundlich, Langmuir), and surface complexation models (e.g., constant capacitance, triple layer) to describe the sorption reactions of heavy metals. For example, the uptake of Ni on montmorillonite, a backfill material used in nuclear waste repositories, has been extensively investigated in our laboratory (Baeyens and Bradbury, 1997), and a "mechanistic" surface complexation model was developed to predict the fate of radionuclides (Bradbury and Baeyens, 1997). However, surface complexation models employ an array of adjustable parameters to fit experimental data, and it has been shown that often, sorption data will fit a number of the models equally well (e.g., Westall and Hohl, 1980). Another major disadvantage of most surface complexation models (and equilibrium-based models in general) is that processes such as precipitation and diffusion are not accounted for. One must realize that equilibrium-based models simply describe macroscopic data and do not definitively prove a reaction mechanism. For these reasons, the uptake of heavy metal on clay minerals has been directly studied at the molecular level by means of extended X-ray absorption fine structure (EXAFS) (O'Day et al., 1994; Scheidegger et al., 1998; Thompson et al., 1999; Dähn et al., 2001, 2002b; Morton et al., 2001; Schlegel et al., 2001a). Uptake mechanisms so far identified on dioctahedral phyllosilicates include the formation of a layered double hydroxide phase and the neoformation of a phyllosilicate phase (Scheidegger et al., 1998; Dähn et al., 2002b).

In a powder EXAFS study, Scheidegger et al. (1998) observed the formation of Ni-Al layered double hydroxide phase on uptake of Ni on pyrophyllite (a dioctahedral 2:1 phyllosilicate that lacks isomorphic substitution). By the use of a combination of powder and polarized EXAFS, Dähn et al. (2002b) observed the neoformation of a Ni-phyllosilicate phase on Ni uptake on montmorillonite (STx-1). In the latter study, polarized EXAFS (P-EXAFS) has been employed because the application of *powder* EXAFS to determine the uptake mechanism of metal ions on clay minerals is limited by the extension of the explored reciprocal space (at best $\Delta k = 14$ Å^{-1}), which precludes the discrimination of atomic shells separated by less than 0.10 to 0.15 Å (Teo, 1986). This is typically the case in phyllosilicates. In montmorillonite, for example, X-ray–absorbing atoms in the octahedral sheet are surrounded by neighboring cations at R $\sim$ 3.00 Å in the octahedral sheet and R $\sim$ 3.15 to 3.23 Å in tetrahedral sheets (Fig. 1). This local structure results in a strong overlap of scattering contributions from the octahedral and tetrahedral cations. Manceau and coworkers showed that this limitation can be overcome by P-EXAFS spectroscopy (Manceau et al., 1988, 1998; Manceau, 1990).

2. P-EXAFS BACKGROUND

In P-EXAFS, neighboring atoms along the polarization direction of the X-ray beam are preferentially probed, and atoms located in a plane perpendicular to this direction are attenuated (Fig. 2). Applying P-EXAFS to montmorillonite self-supporting films has the advantage of minimizing the contributions from the out-of-plane Si atoms from the tetrahedral sheet when the X-ray polarization vector is in the *ab* plane of the montmorillonite self-supporting film. Conversely, when the polarization vector is aligned normal to the film plane, the contribution from octahedral layer cation vanishes.

Originally, P-EXAFS was applied to single-crystal phyllosilicate crystals (Manceau et al., 1988, 1990). More recently, Manceau et al. (1998, 1999) demonstrated that this technique can be extended to fine-grained layered clay minerals. Self-supporting clay films can be prepared by filtration and the angular dependence between the electric field vector $\boldsymbol{\varepsilon}$ and the surface of a self-supporting clay film can be recorded. The angular variations of P-EXAFS spectra depend strongly on how perfectly the *ab* crystallographic planes of individual montmorillonite platelets are aligned parallel to the film surface (Fig. 3). Therefore, quantitative determination of the orientation distribution of individual crystallites in the film is necessary to accurately determine coordination numbers and to localize scattering atoms relative to the polarization direction. The orientation distribution of a film is obtained by X-ray diffraction (see section 4.3).

In P-EXAFS, one detects an apparent coordination number ($CN_{j,\alpha}^{exafs}$), which is the effective number of atoms seen at the angle α and which is modified by the spread of clay particles in the film plane (Manceau and Schlegel, 2001):

$$\frac{CN_{j,\alpha}^{exafs}}{CN_j^{cryst}} = 1 - \frac{(3\cos^2 \beta_j^{cryst} - 1) \cdot (3\cos^2\alpha - 2)}{2} \cdot I_{ord}, \qquad (1)$$

where α is the angle between the $\boldsymbol{\varepsilon}$ vector and the layer plane and β_j^{cryst} is the angle between the film normal and the vector ($\mathbf{R}_{ij}$) connecting the X-ray absorbing atom i to the backscattering atom j, and CN_j^{cryst} is the crystallographic number of atoms in the j shell.

I_{ord} is the function that accounts for the particle disorder; its value is unity for perfectly ordered films and zero for an isotropic sample (Dittmer and Dau, 1998; Manceau and Schlegel, 2001).

I_{ord} is defined as

$$I_{ord} = \frac{\int_0^{\pi/2} (3\cos^2 \alpha - 1)\exp(-\alpha^2 \ln(2)/\Omega^2)\sin \alpha \, d\alpha}{2\int_0^{\pi/2} \exp(-\alpha^2 \ln(2)/\Omega^2) \sin \alpha \, d\alpha}, \qquad (2)$$

with Ω, the half width at half maximum of the mosaic spread

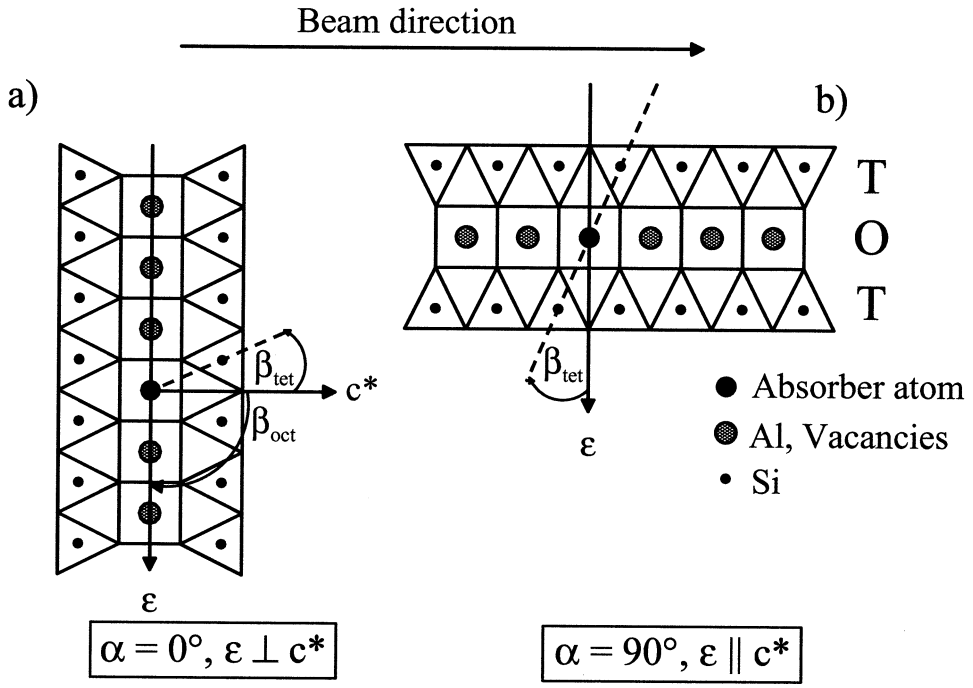

Fig. 2. Orientation of the montmorillonite film with respect to the incoming X-ray beam. (a) Electric field vector $\boldsymbol{\varepsilon}$ parallel to the layer plane. (b) ε perpendicular to the layer plane. After Manceau et al. (1988).

of clay particles of the film plane, obtained from the orientation distribution.

Eqn. 1 can be written as a function of $\cos^2\alpha$:

$$\frac{CN_{j,\alpha}^{exafs}}{CN_j^{cryst}} = \frac{I_{ord}}{2}(3 - 9\cos^2\beta_j^{cryst}) \cdot \cos^2\alpha + 3I_{ord}\cos^2\beta_j^{cryst} + 1 - I_{ord} \quad (3)$$

$$\frac{CN_{j,\alpha}^{exafs}}{CN_j^{cryst}} = \alpha \cdot \cos^2\alpha + b. \quad (4)$$

where a and b are regression coefficients. a can be obtained from a linear regression of $CN_{j,\alpha}^{exafs}/CN_j^{cryst}$ with respect to $\cos^2\alpha$, and the β_j^{cryst} value is obtained from

$$\beta_j^{cryst} = \arccos\sqrt{\left|\frac{3 - 2a/I_{ord}}{9}\right|}. \quad (5)$$

Eqn. 1 can be simplified for two "magic angles": $CN_{j,\alpha}^{exafs} = CN_j^{cryst}$ for $\alpha = 35.3°$, regardless of the value of β and I_{ord}, and for $\beta = 54.7°$, regardless of the value of α and I_{ord}.

3. OBJECTIVES

The objective of this study is to gain direct structural data for adsorbed metal ions on the layer edges of a dioctahedral smectite. The first work of this nature was reported by Schlegel et al. (1999, 2001b) for trioctahedral smectites investigating the uptake of Co and Zn on hectorite. For dioctahedral smectites, however, spectroscopic studies at high surface loadings have so far only demonstrated the presence of layered double hydroxide

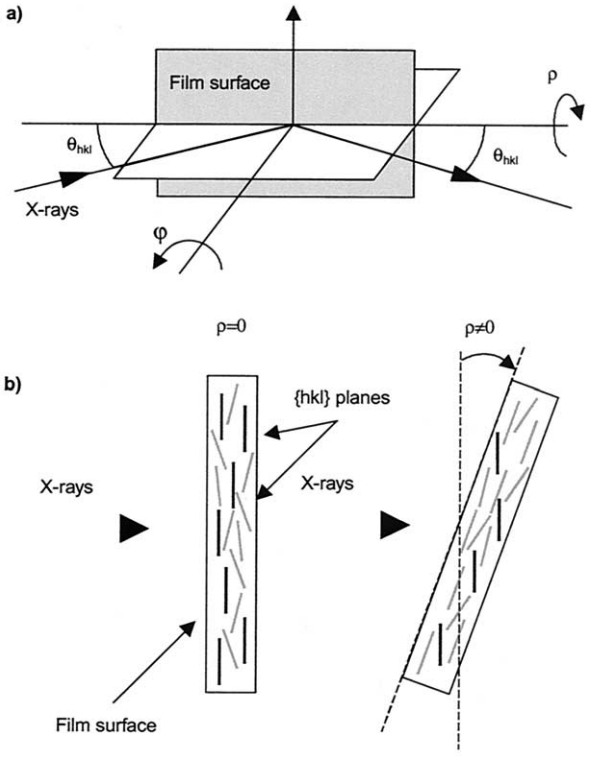

Fig. 3. (a) X-ray diffraction geometry used for texture analysis and (b) a side view of (a) showing how individual crystallographic planes within the film are brought into a diffraction position by a rotation of ρ. After Manceau et al. (1998).

and neoformed Ni-phyllosilicate phases on the uptake of divalent metal ions (Scheidegger et al., 1998; Dähn et al., 2002b).

In this study, the uptake mechanism of Ni on montmorillonite as a function of time at pH 7.2 and low Ni concentrations was investigated with P-EXAFS on dry self-supporting montmorillonite films. The local structure around Ni atoms on montmorillonite was determined, and the possible evolution of the coordination environment of Ni was recorded over a period of up to 1 yr.

4. MATERIALS AND METHODS

4.1. Montmorillonite Purification and Characterization

The montmorillonite STx-1 used in this study was purchased from the Source Clay Minerals Repository of the Clay Minerals Society. X-ray diffraction of the "as-received" montmorillonite indicated the presence of minor quantities of calcite, quartz, and kaolinite amounting to less than ~1 wt%. This natural clay has a total iron content of ~0.9 wt% (expressed as Fe_2O_3). Its structural formula is $Na_{0.05}Ca_{0.15}Mg_{0.03}(Al_{1.5}Fe(III)_{0.1}Mg_{0.4})(Si_4)O10(OH)_2 \cdot n\ H_2O$.

The <0.5 μm montmorillonite fraction used in this study was obtained in a purification and conditioning processes. Briefly, the clay was thoroughly washed three times with 1 mol/L $NaClO_4$ to convert the clay into the homoionic Na form. The <0.5 μm size fraction was selected by successive washing with deionized water combined with centrifugation, and soluble hydroxyaluminium compounds and traces of amorphous iron were removed. Details are given elsewhere (Dähn et al., 2002b). The cation exchange capacity of the conditioned montmorillonite measured by the Ca^{45} isotopic dilution method (Baeyens and Bradbury, 1995a) is 1010 ± 10 meq kg^{-1}. The external surface area of the conditioned STx-1 Ca-montmorillonite was measured by the N_2-BET technique to be 89 $m^2\ g^{-1}$. This value is in agreement with that determined by Van Olphen and Fripiat (1979) (84 $m^2\ g^{-1}$).

4.2. Sample Preparation for P-EXAFS

The P-EXAFS samples were prepared by adding 200 mL of a buffered Ni solution (pH 7.2, [Ni] = 23.8 μM, 0.3 mol/L $NaClO_4$) to 40 mL of a conditioned and purified Na-montmorillonite suspension (pH 7.0, 0.3 mol/L $NaClO_4$; Baeyens and Bradbury, 1997). The resulting solid-to-liquid ratio was 2.2 g/L, and the initial Ni concentration ($[Ni]_{initial}$) was 19.9 μM. It has been shown previously that the use of the buffer (8.3 mM (3-(*N*-Morpholino) propanesulfonic acid) to maintain constant pH did not influence Ni uptake on montmorillonite (Baeyens and Bradbury, 1995b). Experiments were carried out with high-ionic-strength Na background electrolyte to block cation exchange sites. The Ni uptake experiments were conducted at room temperature in a glove box under N_2 atmosphere (CO_2 and O_2 <5 ppm).

After 14 and 360 d of reaction time, 40 mL of the suspensions were slowly filtrated through 47-mm-diameter filters (Millipore, 0.4 μm pore size), and two highly oriented self-supporting films were prepared. The filtration was performed in a closed vessel under a continuous flow of argon. Excess of solution in the wet films was removed by washing with a few milliliters of deionized water before air drying at room temperature. The filtered solution was analyzed for Ni, Si, and Al by optical emission spectroscopy (ICP-OES). The Ni weight concentration in the clay films was low enough (<0.05 wt%) to neglect self-absorption effects (Tröger et al., 1992; Castañer and Prieto, 1997). The dried clay films were cut into slices and were then stacked on a sample holder to obtain a sufficient thickness for fluorescence measurements. In a previous study, we verified that the drying of the film did not modify the overall coordination chemistry of Ni (Dähn et al., 2002b).

Because the goal of this study was to investigate the sorption of Ni on montmorillonite, we selected reaction conditions ($[Ni]_{initial}$ = 19.9 μM, pH = 7.2) under which the formation of Ni-Ni nucleation products such as $NiOH_2$ should not occur but which would nevertheless allow assessable EXAFS data to be obtained (see section 5.3). To our knowledge, the solubility products of Ni-silicate phases (e.g., Ni phyllosilicates) are not known. The log $K_{sp}^{Ni(OH)_2}$ values reported in the literature vary over a wide range (-10.52 to -18.06; Britton, 1925; Mattigod et al., 1997; Plyasunova et al., 1998). To estimate the degree of saturation with respect to the solubility of $Ni(OH)_2$, the saturation index (SI) was calculated. SI is defined as the ratio of the ion activity product, IAP, to the solubility constant K_{sp}. This yields $SI = (Ni^{2+})/[(H^+)^2 \cdot K_{sp}]$, where (Ni^{2+}) and (H^+) are the activities of Ni^{2+} and H^+ in solution. The calculation indicated that $[Ni]_{initial}$ was clearly below the solubility limit of $Ni(OH)_2$ ($SI < 0.06$, with log $K_{sp}^{Ni(OH)_2} = -10.52$, Plyasunova et al., 1998; $SI < 2 \times 10^{-9}$, with log $K_{sp}^{Ni(OH)_2} = -18.06$, Britton, 1925). Thus, one can assume that Ni removal from solution is not due to $Ni(OH)_2$ formation in solution at any time during the experiments.

Ni speciation calculated with the thermodynamic data in Baes and Mesmer (1976) showed that under the reaction conditions employed ($[Ni]_{initial}$ = 19.9 μM, pH = 7.2), Ni(II) was almost completely present as Ni^{2+} (aq). The concentrations of hydrolyzed species such as $Ni(OH)^+$, $Ni(OH)_2^0$, $Ni(OH)_3^-$, $Ni(OH)_4^{2-}$, $Ni_2(OH)^{3+}$, and $Ni(OH)_4^{4+}$ were, altogether, $< 2 \times 10^{-8}$ M.

4.3. Quantitative Texture Analysis

X-ray diffraction texture analysis measurements were conducted with Ni-treated self-supporting montmorillonite films with a Huber texture goniometer in reflection mode, with monochromatized Cu K_α radiation collimated to a 0.5×0.5–mm parallel beam. The complete film texture can be obtained by measuring the inclination of {001} crystallographic planes off the sample surface (Manceau et al., 1998). Figure 3a illustrates the principle of obtaining the film texture on a diffractometer. Three rotation movements Bragg angle (θ_{hkl}), azimuthal (φ), and tilt angle (ρ) are available. For a fixed θ_{hkl}, all platelets are brought into a diffracting position by rotating the sample around φ and ρ. However, in such films, textures are axially symmetric around the normal to the film plane (Manceau et al., 1998), and thus only a ρ scan is necessary to obtain the full orientation information. The diffracted intensity is proportional to the number of montmorillonite planes satisfying the Bragg condition at these orientations. Figure 3b illustrates how individual particles are brought into diffracting position (black planes are diffracting).

We have measured (004) pole figures of a single slice of the montmorillonite film by scanning ρ between 0 and 85° with angle increments of 5° and an integration time of 2 h for each tilt angle position. The densities of the orientation distribution were calculated from the diffracted intensities integrated over all ρ angles by means of direct normalization and taking a density of zero for $\rho > 80°$ (for details, see Manceau et al., 1998). Distribution densities are expressed as multiple of a random distribution, or mrd (Bunge and Esling, 1982), and are equal to 1 for a randomly orientated sample.

4.4. EXAFS Data Collection and Reduction

Ni K-edge XAFS spectra were recorded on the ID26 beamline at the European Synchrotron Radiation Facility, Grenoble, France (Gauthier et al., 1999). All spectra were recorded at room temperature using a Si(220) monochromator and a fast, highly linear, and low-noise silicon photodiode with a 6 μm thick Co filter (Gauthier et al., 1996). Higher-order harmonics were rejected with two mirrors (Si and fused silica, Signorato and Solé, 1999). The monochromator angle was calibrated by assigning the first inflection point of the K-absorption edge spectrum of Ni metal to 8333 eV. P-EXAFS spectra were recorded with the electric field vector $\boldsymbol{\varepsilon}$ at $\alpha = 10$, 35, 55, and 80° with respect to the film plane. Several scans were averaged to improve the signal-to-noise ratio.

Data reduction was carried out with the WinXAS 97 2.1 software package (Ressler, 1998). The energy was converted to photoelectron wave vector units ($Å^{-1}$) by assigning the origin E_0 to the first inflection point of the absorption edge. Radial structure functions (RSFs) were obtained by Fourier transforming k^3-weighted $\chi(k)$ functions between 3.2 and 10 $Å^{-1}$ with a Bessel window function with a smoothing parameter of 4. Amplitude and phase shift functions were calculated with FEFF 8.0 (Rehr et al., 1991); we used the structures of β-$Ni(OH)_2$ and Ni-Talc (Perdikatsis and Burzlaff, 1981) as references. Fits were performed in R space in the 0.6 to 3.5 Å interval. The amplitude reduction factor (S_0^2) was determined to be 0.85 from the experimental

β-Ni(OH)$_2$ EXAFS spectrum. The deviation between the fitted and the experimental spectra (%Res) is given by

$$\%\mathrm{Res} = \frac{\sum_{i=1}^{N} |y_{\mathrm{exp}}(i) - y_{\mathrm{theo}}(i)|}{\sum_{i=1}^{N} y_{\mathrm{exp}}(i)} \cdot 100, \quad (6)$$

where N is the number of points in the fit window, and y_{exp} and y_{theo} are the experimental and theoretical RSF values. The precision on the P-EXAFS distances (R) was previously estimated to be $\leq \pm 0.02$ Å for $R_{\mathrm{Ni\text{-}O}}$, $\leq \pm 0.03$ Å for $R_{\mathrm{Ni\text{-}Al}}$ and $R_{\mathrm{Ni\text{-}Si}}$, and ± 0.5 for the coordination numbers (CN^{exafs}) (Dähn et al., 2002b; Schlegel et al., 2001b). The experimental uncertainty on α in the P-EXAFS measurements is $\leq \pm 1°$.

5. RESULTS

5.1. Ni Uptake Experiments

ICP-OES measurements showed that the proportion of Ni taken up amounted to 46% of the initial Ni concentration (4 μmol/g, $[\mathrm{Ni}]_{\mathrm{eq}} = 10.8$ μM) after 14 d and 83% (7 μmol/g, $[\mathrm{Ni}]_{\mathrm{eq}} = 3.3$ μM) after 360 d of reaction time. The Si concentration in solution increased from 110 to 320 μM, corresponding to an average Si release rate of 4.4×10^{-14} mol m^{-2} s^{-1} (pH = 7.2; time range, 14 to 360 d). The measured Si release rate agrees with dissolution rates of montmorillonite in the presence (3.5×10^{-14} mol m^{-2} s^{-1}, pH = 8.0; time 14 to 206 d, Dähn et al., 2002b; 3.2×10^{-14} mol m^{-2} s^{-1}, pH = 7.5, Scheidegger et al., 1997) and absence of Ni (5.4×10^{-14} mol m^{-2} s^{-1}, pH = 5, Furrer et al., 1993; and 1×10^{-15} mol m^{-2} s^{-1}, pH = 6, Heydemann, 1966). The Al and Mg concentration in solution was too low (<4 μM) to produce reliable ICP-OES measurements.

5.2. Texture Analysis

Intensities of ρ scans were obtained by averaging for each ρ value the normalized densities of (004) pole figures. The variations of the diffracted intensity of the (004) reflection are shown in Figures 4 a,b for 14- and 360-d reaction times, respectively.

At $\rho = 0$, we observe a strong maximum with a density value of approximately 10 mrd (14-d reaction time) and 8.4 mrd (360-d reaction time), which indicates that most of the montmorillonite platelets have their (*a*,*b*) planes aligned parallel to the film plane. The experimental ρ-scan curves were best-fitted with gaussian distributions (solid line in Fig. 4). The fit resulted in a full width at half maximum (FWHM) of 44.3° for the sample that was in contact with Ni for 14 d, and a FWHM of 47.1° for 360 d. These texture values will be used later to correct the coordination numbers and the experimentally determined β angles for the imperfect orientation by Eqns. 1 and 5 (see section 5.3).

5.3. P-EXAFS

Figures 5 a,b show k $^3\chi$(k) P-EXAFS spectra of Ni-treated self-supporting montmorillonite films recorded at various angles for reaction times of 14 and 360 d, respectively. The

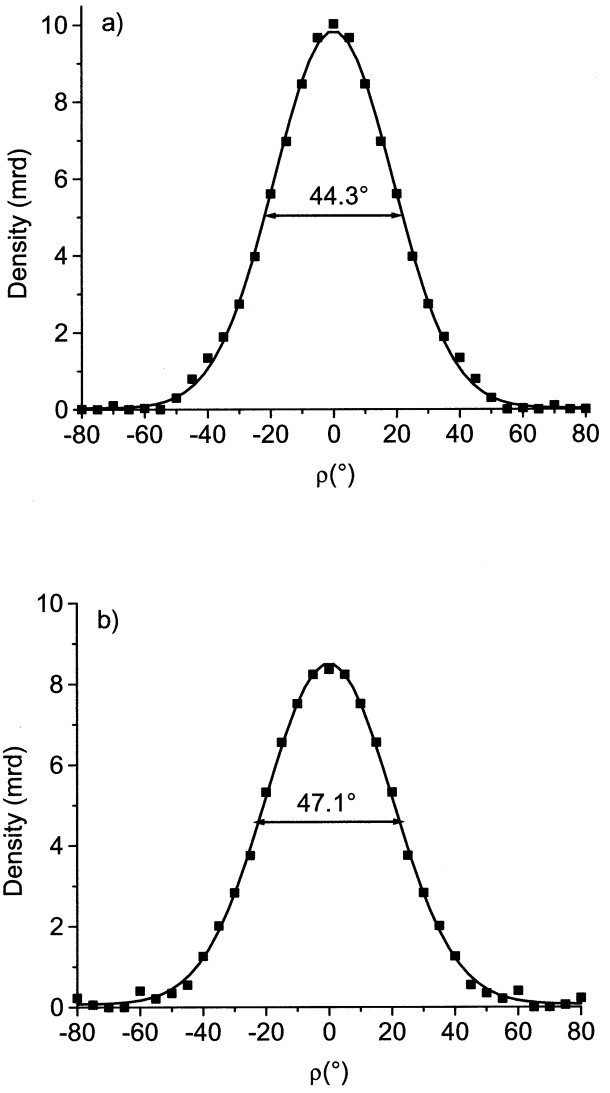

Fig. 4. Integrated radial distribution densities of the c* axes of montmorillonite crystals with respect to the normal of the film plane (ρ = 0°) for (a) 14-d and (b) 360-d reaction time.

figures exhibit a pronounced angular dependence, consistent with a successful film preparation (see section 5.2). The two spectra recorded at $\alpha = 80°$ have a clear beat pattern at k = 5.3 Å^{-1}. With increasing α angle, the intensity of the shoulder at 5.3 Å^{-1} increases, and the wave frequency at 5.3 Å^{-1} shifts slightly. The spectra contain several isosbestic points, for which k$^3\chi$(k) is independent of α. Isosbestic points are very sensitive to normalization errors during the reduction of raw X-ray absorption spectra. The fact that all the individual k$^3\chi$(k,α) spectra precisely cross at the same value in these points provides a stringent proof of the reliability of P-EXAFS spectra even at high k values, where the noise is the highest.

The changes in spectral shape and frequency indicate that the coordination chemistry of Ni is anisotropic—that is, its coordination environment is oriented with respect to clay layers. Furthermore, the anisotropy in the spectra is increasing with increasing reaction time (Fig. 5a, 14-d data, and Fig. 5b, 360-d

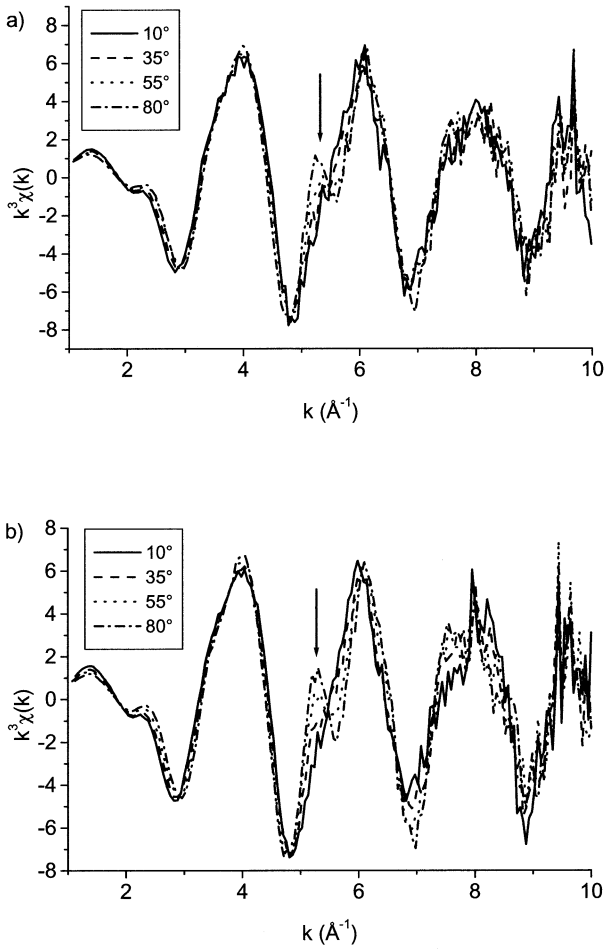

Fig. 5. k^3-weighted Ni K-edge P-EXAFS spectra of a Ni-treated montmorillonite film (pH 7.2) at α angles of 10, 35, 55, and 80°. The arrows indicate the most important anisotropic spectral feature. (a) 14-d reaction time (4 μmol/g) and (b) 360-d reaction time (7 μmol/g).

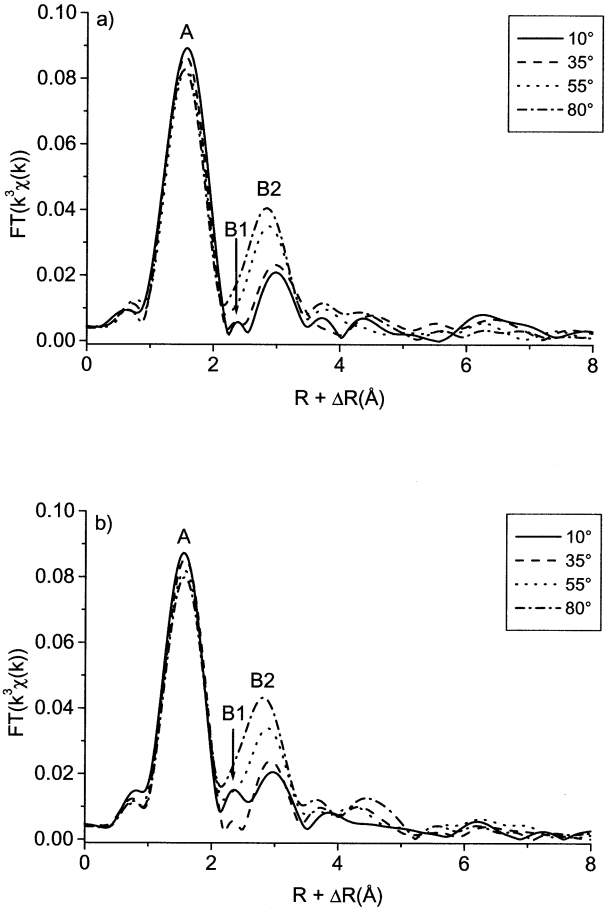

Fig. 6. Polarization dependence of the RSFs obtained from the EXAFS spectra presented in Figure 5. (a) 14-d reaction time (4 μmol/g); (b) 360-d reaction time (7 μmol/g). The arrows indicate peak B1.

data), suggesting that the average coordination environment of Ni is modified with time.

In the corresponding experimental RSFs for 14- and 360-d reaction times (Figs. 6a,b, respectively), there is a RSF peak (Ni-O contribution) at 1.54 Å in both samples (labeled A). With increasing α angle, the amplitude of peak A decreases while the peak position remains constant. Beyond the first shell, there are two further RSF peaks (labeled B1 and B2). Furthermore, Figure 6 shows that most of the anisotropy observed in the α-$k^3\chi$(k) spectra is transferred to the RSF peaks B1 and B2 in the real space. Peak B2 is present at all angles and for both reaction times, whereas peak B1 ($R + \Delta R = 2.35$ Å, $\alpha = 10°$) is only clearly resolved after a reaction time of 360 d. With increasing α, the intensity of peak B2 is increasing and the position shifts from $R + \Delta R = 2.98$ Å ($\alpha = 10°$) to $R + \Delta R = 2.84$ Å ($\alpha = 80°$).

Peak B1 can either correspond to a side-lobe peak, originating from the limited reciprocal space integrated in the Fourier transform (FT) (i.e., a truncation effect), or it may have a structural origin. The first hypothesis can be disregarded for the following reasons. First, a parameterized Bessel function was used, which minimizes the intensity of a side lobe (see section 4.4). Second, for a given Fourier-integration range, the ratio of intensities of the main and side-lobe peaks is constant. Thus, when the intensity of peak A remains constant, the intensity of peak B1 should remain constant also. Examination of Figure 6 shows that the intensities of peak A remained unchanged for $\alpha = 10°$ (solid line, Fig. 6), whereas the intensity of peak B1 increased with time (14 vs. 360 d). Finally, the peak B2 is asymmetric on its left side, suggesting that a further backscattering contribution is present at a shorter distance. The fact that peak B1 is most pronounced at $\alpha = 10°$ demonstrates the ability of P-EXAFS to probe especially the local order beyond the first coordination shell, which is precisely the scale needed to determine surface complexes formed on Ni uptake on montmorillonite.

Structural parameters derived from a multishell fit in R-space are reported in Table 2 (14-d data) and Table 3 (360-d data). As an example the fitted FTs for the 360-d data are shown in Figure 7, together with the experimental data of the Ni-treated montmorillonite film. The figure indicates that the fits match the experimental data well for both the real and the imaginary parts. Furthermore, Figure 7 shows that the imaginary part is strongly depending on the α angle. The angular evolution of the modulus and the imaginary part indicates that the sorbed Ni has

Table 2. Structural information derived from P-EXAFS analysis for the 14-day sample.[a]

	Ni-O shell			Ni-Al shell			Ni-Si1 shell			Ni-Si2 shell				
α	CN^{exafs}_{Ni-O}	R_{Ni-O} (Å)	σ^2 (Å^2)	CN^{exafs}_{Ni-Al}	R_{Ni-Al} (Å)	σ^2 (Å^2)	CN^{exafs}_{Ni-Si1}	R_{Ni-Si1} (Å)	σ^2 (Å^2)	CN^{exafs}_{Ni-Si2}	R_{Ni-Si2} (Å)	σ^2 (Å^2)	ΔE_0 (eV)	%Res
10°	5.5	2.03[b]	0.005[b]	2	3.00[c]	0.006[c]	1.3	3.10[d]	0.006[c]	3.5	3.27[d]	0.006[c]	−0.1[b]	9.8
35°	5.3	2.03	0.005	1.6	3.00[c]	0.006[c]	1.9	3.10[d]	0.006[c]	4.4	3.27[d]	0.006[c]	−0.1	10.1
55°	5.0	2.03[b]	0.005[b]	0.9	3.00[c]	0.006[c]	2.6	3.10[d]	0.006[c]	5.6	3.27[d]	0.006[c]	−0.1[b]	8.0
80°	4.8	2.03[b]	0.005[b]				3.0	3.10	0.006[c]	6.3	3.27	0.006[c]	−0.1[b]	8.3

[a] CN^{exafs}, R, σ^2, ΔE_0 are the apparent coordination numbers, interatomic distances, Debye-Waller factors, and inner potential corrections, respectively.
[b] Fixed to the value determined at $\alpha = 35°$.
[c] Fixed to the value obtained from the P-EXAFS analysis for the 360-day sample (Table 3).
[d] Fixed to the value determined at $\alpha = 80°$.

a different local structure parallel and perpendicular to the montmorillonite film plane.

Data analysis indicated that the first coordination shell is described best by O atoms at a bond distance (R_{Ni-O}) of 2.05 Å, which is typical of sixfold coordinated Ni (Pandya et al., 1990). To reduce the number of fit parameters R_{Ni-O}, σ^2_{Ni-O} and the inner potential correction parameter, ΔE_o, were determined at $\alpha = 35°$, and then held fixed at $\alpha \neq 35°$. It was not possible to fit any of the experimental data using a Ni-Ni pair or a combination of Ni-Ni and Ni-Si/Al pairs. This finding suggests that no Ni nucleation phase (e.g., $NiOH_2$, Ni phyllosilicates) formed in our sorption system under the employed reaction conditions. Furthermore, any attempts to fit the second FT peak with a single Ni-Si pair failed, and a good fit with two Ni-Si pairs (Ni-Si1/Ni-Si2) was obtained only at $\alpha = 80°$. To reduce the number of fit parameters further, the following EXAFS parameters were constrained at α angles different from 80°: R_{Ni-Si1}, σ^2_{Ni-Si1}, R_{Ni-Si2} and σ^2_{Ni-Si2} were fixed to their values at $\alpha = 80°$.

Following the constrains described above, the second FT peak at $\alpha \neq 80°$ could be fitted well with one Ni-Al and two Ni-Si pairs for both samples (Table 2, 14-d data, and Table 3, 360-d data). In contrast to the Ni-Si pairs, which were detected at all angles, the Ni-Al pair was completely extinguished in the perpendicular orientation in both samples. With increasing angle, CN^{exafs}_{Ni-A1} at 3.00 Å decreased (e.g., from CN^{exafs}_{Ni-Al} (360 d) $= 2.8 \pm 0.5$ at $\alpha = 10°$ to CN^{exafs}_{Ni-A1} (360 d) $= 1 \pm 0.5$ at $\alpha = 55°$) whereas CN^{exafs}_{Ni-Si1} at 3.10 to 3.12 Å and CN^{exafs}_{Ni-Si2} at 3.26 to 3.27 Å increased (e.g., from CN^{exafs}_{Ni-Si1} (360 d) $= 0.7 \pm 0.5$ and CN^{exafs}_{Ni-Si2} (360 d) $= 3.4 \pm 0.5$ at $\alpha = 10°$ to CN^{exafs}_{Ni-Si1} (360 d) $= 2.5 \pm 0.5$ and CN^{exafs}_{Ni-Si2} (360 d) $= 5.5 \pm 0.5$ at $\alpha = 80°$) in both samples.

The sum of experimentally determined $CN^{exafs}_{Ni-Si1} + CN^{exafs}_{Ni-Si2}$ can be compared with the sum of nearest Si neighbors of cations (Al, Mg, Fe) in the octahedral sheet of montmorillonite. The crystallographic value for $CN^{cryst}_{Ni-Si1} + CN^{cryst}_{Ni-Si2}$ in montmorillonite is 4 (Table 1). By using Eqn. 1 and assuming crystallographic β values of phyllosilicates ($\beta^{cryst} = 33$–$35°$) and $\alpha = 80°$ one expects the sum of $CN^{cryst}_{Ni-Si1,\alpha=80°} + CN^{cryst}_{Ni-Si2,\alpha=80°}$ to become ~8 (Table 1). This crystallographic value corresponds well with the coordination number of Si1 and Si2 determined experimentally at $\alpha = 80°$ ($CN^{exafs}_{Ni-Si1,\alpha=80°} + CN^{exafs}_{Ni-Si2,\alpha=80°}$ ~8, 360-d data). With decreasing α, the correspondence between crystallographic and experimental values for the sum of Si neighbors decreases. For example, for $\alpha = 35°$, the coordination number of Si1 and Si2 ($CN^{exafs}_{Ni-Si1,\alpha=35°} + CN^{exafs}_{Ni-Si2,\alpha=35°}$ ~5.5, 360-d data) is slightly higher than those expected in phyllosilicates ($CN^{cryst}_{Ni-Si1} + CN^{cryst}_{Ni-Si2} = 4$). We suspect that the reason for the increasing disagreement for angles $\alpha < 80°$ is caused by the Ni-Al pair at $R_{Ni-Al} = 3.0$ Å, which contributes to the overall spectrum. A FEFF simulation supports this hypothesis and indicates that Ni-Al pairs at 3.0 Å are destructively interfering with the two Ni-Si pairs (at 3.1 to 3.12 Å and 3.26 to 3.27 Å).

On the basis of the variation of CN as function of α, it is possible to experimentally determine the angle β between the

Table 3. Structural information derived from P-EXAFS analysis for the 360-day sample.

	Ni-O shell			Ni-Al shell			Ni-Si1 shell			Ni-Si2 shell				
α	CN^{exafs}_{Ni-O}	R_{Ni-O} (Å)	σ^2 (Å^2)	CN^{exafs}_{Ni-Al}	R_{Ni-Al} (Å)	σ^2 (Å^2)	CN^{exafs}_{Ni-Si1}	R_{Ni-Si1} (Å)	σ^2 (Å^2)	CN^{exafs}_{Ni-Si2}	R_{Ni-Si2} (Å)	σ^2 (Å^2)	ΔE_0 (eV)	%Res
10°	5.2	2.04[b]	0.005[b]	2.8	3.00	0.006[c]	0.7	3.12[a]	0.006[a]	3.4	3.26[a]	0.006[a]	0.2[b]	9.7
35°	5.1	2.04	0.005	2	3.00[d]	0.006[c]	1.5	3.12[a]	0.006[a]	4	3.26[a]	0.006[a]	0.2	6.9
55°	5	2.04[b]	0.005[b]	1	3.00[d]	0.006[c]	2	3.12[a]	0.006[a]	4.8	3.26[a]	0.006[a]	0.2[b]	8.0
80°	4.9	2.04[b]	0.005[b]				2.5	3.12	0.006	5.5	3.26	0.006	0.2[b]	7.5

[a] Fixed to the value determined at $\alpha = 80°$.
[b] Fixed to the value determined at $\alpha = 35°$.
[c] Fixed to the value obtained for the Si1 shell.
[d] Fixed to the value determined at $\alpha = 10°$.

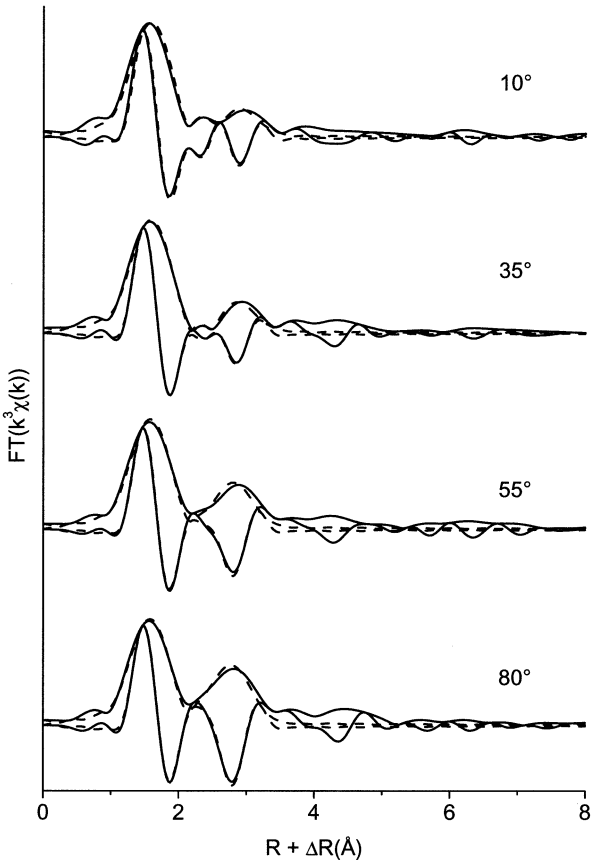

Fig. 7. Polarization dependence of the FTs (modulus and imaginary parts) and the corresponding least-squares fit for the 360-d sample. Solid line = experimental data; dotted line = least-squares fit.

film normal and the vector connecting the X-ray–absorbing atom (Ni) to the backscattering atoms (Si and Al) (see section 2 and Fig. 2). $CN^{exafs}_{Ni\text{-}Al}$, $CN^{exafs}_{Ni\text{-}Si1}$ and $CN^{exafs}_{Ni\text{-}Si2}$ for the Al and Si shells for the 14- and 360-d samples are plotted as a function of $\cos^2\alpha$ in Figure 8 and Figure 9, respectively. Good linear correlations were obtained with regression coefficients $r^2 > 0.99$. The gradual decrease of $CN^{exafs}_{Ni\text{-}Al}$ and increase of $CN^{exafs}_{Ni\text{-}Si1}$ and $CN^{exafs}_{Ni\text{-}Si2}$ with increasing α implies that $\beta_{Ni\text{-}Al} > 54.7°$, and $\beta_{Ni\text{-}Si1}$ and $\beta_{Ni\text{-}Si2} < 54.7°$ (see section 2, Eqn. 1).

In a next step, the β angles for Ni-Al, Ni-Si1, and Ni-Si2 pairs were then calculated by Eqn. 5. Assuming a perfectly ordered film ($I_{ord} = 1$), this approach yields for example for the 360-d data: $\beta_{Ni\text{-}Al} = 84°$, $\beta_{Ni\text{-}Si1} = 39°$, and $\beta_{Ni\text{-}Si2} = 47°$ (Table 4). In reality, some of the montmorillonite platelets in our sorption system are oriented off the film plane (Fig. 4). The values of the mosaic spread of the self-supporting films determined with quantitative texture analysis allow the experimentally determined β angles to be corrected for the imperfect orientation by Eqn. 5. Eqn. 2 was solved numerically because the integral in the numerator has no analytical solution (Manceau and Schlegel, 2001). This resulted in $I_{ord} = 0.73$ (14-d data, FWHM 44.3°) and 0.70 (360-d data, FWHM 47.1°). The corrected β values (β^{real}) are shown in Table 4. The results indicate that Ni-Al pairs are oriented essentially parallel to the film plane and Ni-Si pairs are inclined out of the plane. The

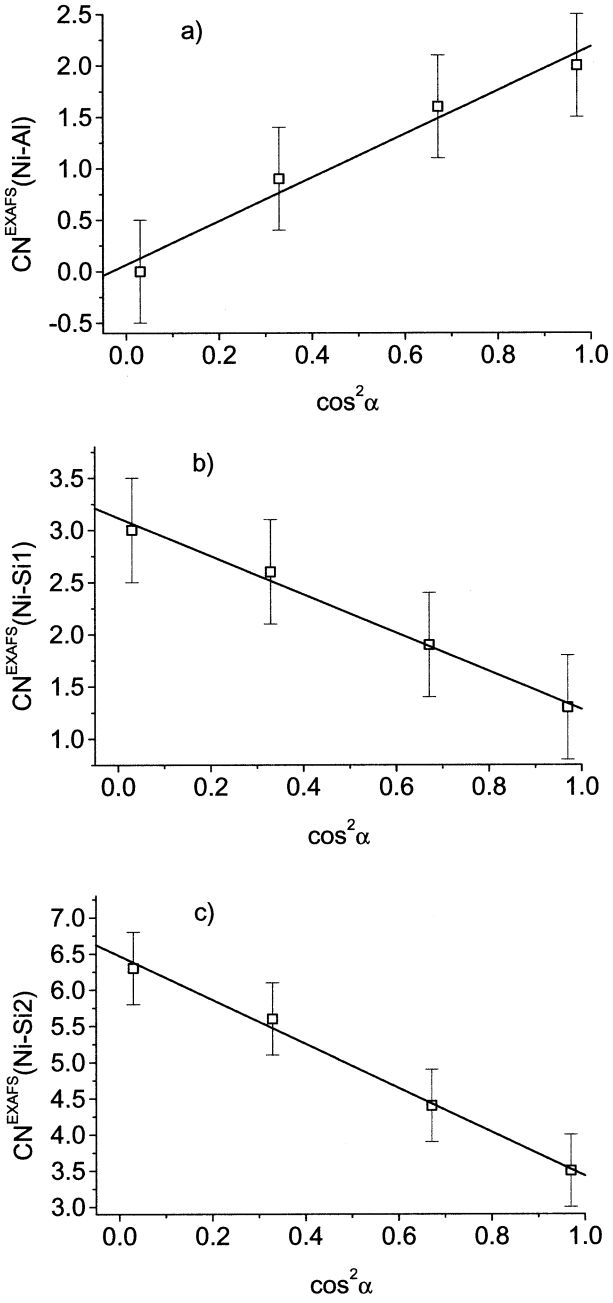

Fig. 8. Angular dependence of $CN^{exafs}_{Ni\text{-}Al}$ (a), $CN^{exafs}_{Ni\text{-}Si1}$ (b), and $CN^{exafs}_{Ni\text{-}Si2}$ (c) for 14-d reaction time. Open squares = experimental data; solid line = linear regression. $CN^{exafs}_{Ni\text{-}Al} = 2.2_1 \cdot \cos^2\alpha$; $CN^{exafs}_{Ni\text{-}Si1} = -1.8_4 \cdot \cos^2\alpha + 3.1_2$; and $CN^{exafs}_{Ni\text{-}Si2} = -3.0_4 \cdot \cos^2\alpha + 6.4_7$ (solid lines). The uncertainty on CN is estimated to be ±0.5.

experimental β angles roughly match with crystallographic values in montmorillonite (33° [trans sites] and 35° [cis sites]; Tsipursky and Drits, 1984).

Because at $\alpha = 10°$ three contributions (Ni-Al, Ni-Si1, and Ni-Si2) are overlapping at a distance between 3.0 to 3.27 Å, it is desirable to obtain further proof for the presence and the intensity of the Ni-Al pair in the continuity of the octahedral sheet. The Al contributions at $\alpha = 10°$ can be calculated from the knowledge of the β angles ($\beta^{real}_{Ni\text{-}Si1}$ and $\beta^{real}_{Ni\text{-}Si2}$), and the

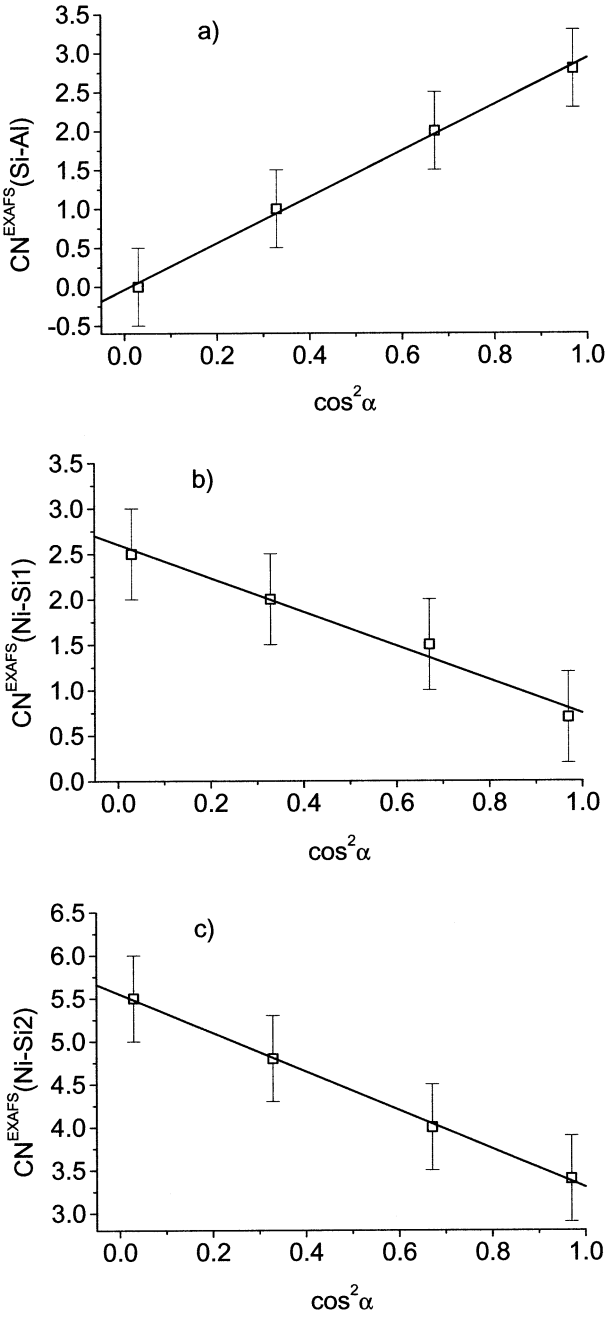

Fig. 9. Angular dependence of $CN^{exafs}_{Ni\text{-}Al}$ (a), $CN^{exafs}_{Ni\text{-}Si1}$ (b), and $CN^{exafs}_{Ni\text{-}Si2}$ (c) for 360-d reaction time. Open squares = experimental data; solid line = linear regression. $CN^{exafs}_{Ni\text{-}Al} = 2.9_2 \cdot \cos^2\alpha$; $CN^{exafs}_{Ni\text{-}Si1} = -1.8_6 \cdot \cos^2\alpha + 2.6_1$; and $CN^{exafs}_{Ni\text{-}Si2} = -2.2_5 \cdot \cos^2\alpha + 5.5_5$ (solid lines). The uncertainty on CN is estimated to be ±0.5.

coordination numbers ($CN^{exafs}_{Ni\text{-}Si1}$ and $CN^{exafs}_{Ni\text{-}Si2}$) of the Ni-Si pairs at $\alpha = 80°$ by Eqn. 1.

In a first approach, we have used theoretical crystallographic values ($\beta^{cryst}_{Ni\text{-}Si1} = 33°$ and $\beta^{cryst}_{Ni\text{-}Si2} = 35°$) for the subtraction of the Si1 and Si2 contribution at $\alpha = 10°$. The Si1 and Si2 contributions were attenuated by 24 and 27% of its amplitude at $\alpha = 80°$. For both samples, this approach yielded $CN^{exafs}_{Ni\text{-}Si1,\alpha=10°} = 0.6$ to 0.7 and $CN^{exafs}_{Ni\text{-}Si2,\alpha=10°} = 1.5$ to 1.7.

Table 4. Reduced slope of linear regressions and inclination of cationic shell from the second FT peak.[a]

Samples	Atomic shell	S	β^{exp}	$\Delta\beta^{exp}$	β^{real}
14 days	Al	1.38	81	9	90[b]
	Si1	−0.97	42	6	38
	Si2	−0.69	46	6	42
360 days	Al	1.46	84	8	90[b]
	Si1	−1.24	39	7	32
	Si2	−0.56	47	7	44

[a] S = slope of the regression line normalized by $CN^{exafs}_{\alpha=35°}$; β^{exp} = inclination angle of the backscattering shell uncorrected for the film texture; $\Delta\beta^{exp}$ = precision on β, estimated from the dispersion of $CN^{exafs}_{j,\alpha}$ at the 95% confidence level; β^{real} = inclination angle of the backscattering shell corrected for the film texture.

[b] The correction for texture effects yielded β^{real} values >90°. These β^{real} values were bounded to maximum (90°) realistic values.

We noted that the subtraction of the Si contributions in this approach was not sufficient to completely remove the Si contributions from the spectra at $\alpha = 10°$. Therefore, we have disregarded the approach by use of crystallographic β values and used instead β^{real} angles determined experimentally (Table 4). Accordingly, the amplitude of the Ni-Si1 and Ni-Si2 shells at $\alpha = 10°$ was attenuated by 33 and 43% of its value at $\alpha = 80°$ for the 14-d data, and 23 and 50% for 360-d data, respectively. These reduction factors were then used to calculate $CN^{exafs}_{Ni\text{-}Si1,\alpha=10°}$ and $CN^{exafs}_{Ni\text{-}Si2,\alpha=10°}$ ($CN^{exafs}_{Ni\text{-}Si1,\alpha=10°} = 1.0$ and $CN^{exafs}_{Ni\text{-}Si2,\alpha=10°} = 2.7$ for 14-d data; $CN^{exafs}_{Ni\text{-}Si1,\alpha=10°} = 0.6$ and $CN^{exafs}_{Ni\text{-}Si2,\alpha=10°} = 2.8$ for 360-d data) and to subtract the contribution of Si atoms in the parallel orientation from the original spectrum at $\alpha = 10°$. The RSFs obtained by this subtraction procedure are shown in Figure 10, together with the original spectrum. The figure shows that the features observed in the 2.2 to 3.5 Å R-range in the original spectrum are caused by an interference of the Ni-Al and Ni-Si pairs. Figure 11 shows the experimental FT after the removal of the Si contribution together with the corresponding fit. The fit shows a good match for the Ni-Al pair (also in the imaginary part). The corresponding fit results are presented in Table 5. The table shows that $CN^{exafs}_{Ni\text{-}Al,\alpha=10°}$ varies between 1.5 and 2.3. When $\sigma^2_{Ni\text{-}Al}$ was fixed to the value obtained for the 360-d sample ($\sigma^2_{Ni\text{-}Al} = 0.005$) $CN^{exafs}_{Ni\text{-}Al,\alpha=10°}$ for the 14-d sample was 1.5. When $\sigma^2_{Ni\text{-}Al}$ of the 14-d sample was allowed to vary, $\sigma^2_{Ni\text{-}Al}$ increased from 0.005 Å^2 to 0.01 Å^2 and $CN^{exafs}_{Ni\text{-}Al,\alpha=10°}$ (14-d sample) increased from 1.5 to 2.2. Thus, the fit results can be interpreted by either $\sigma^2_{Ni\text{-}Al}$ decreasing or $CN^{exafs}_{Ni\text{-}Al,\alpha=10°}$ increasing with increasing reaction time. To determine $CN^{cryst}_{Ni\text{-}Al}$ for the following discussion we have applied Eqn. 1 to the $CN^{exafs}_{Ni\text{-}Al,\alpha=10°}$ obtained by the subtraction procedure (with $\beta = 90°$, $I_{ord} = 0.79$ [14-d data] and 0.77 [360-d data]). This result for the 14-d data in: $CN^{cryst}_{Ni\text{-}Al}$ (14 d) = 1.5 ($\sigma^2_{Ni\text{-}Al} = 0.01$ Å^2), and $CN^{cryst}_{Ni\text{-}Al} = 1$ ($\sigma^2_{Ni\text{-}Al} = 0.005$ Å^2) and for the 360-d data: $CN^{cryst}_{Ni\text{-}Al} = 1.6$ ($\sigma^2_{Ni\text{-}Al} = 0.005$ Å^2). The obtained $CN^{cryst}_{Ni\text{-}Al}$ compare well with the values of the multi-shell fit with two Si shells (e.g., for 360 d $CN^{cryst}_{Ni\text{-}Al} = 1.6$ vs. $CN^{exafs}_{Ni\text{-}Al,\alpha=35°} = 2$; Table 3). The above data analysis approach demonstrates how P-EXAFS allow the discrimination between contributions of overlapping atomic shells to be improved and

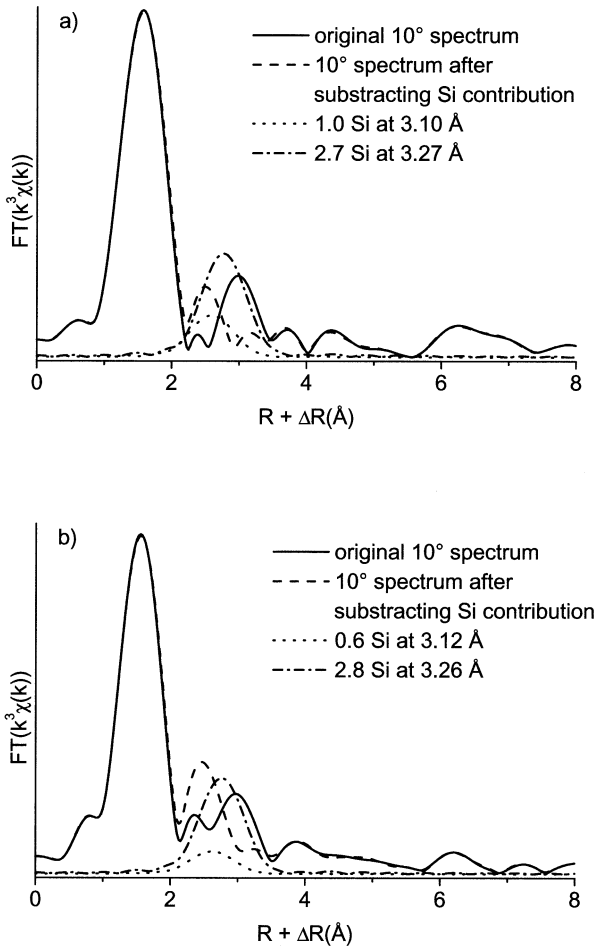

Fig. 10. RSF of the original 10° spectrum (solid line) and the 10° spectrum after subtraction (dashed line) of the contribution of Si1 (dotted line) and Si2 (dash dotted line). (a) 14-d and (b) 360-d reaction times.

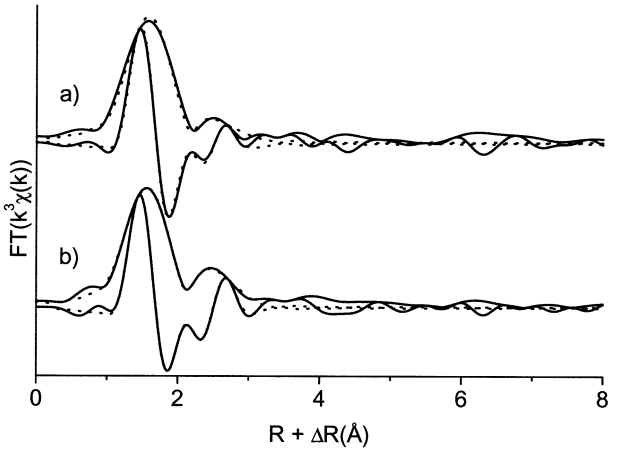

Fig. 11. FTs (modulus and imaginary parts) and the corresponding least-squares fit for (a) the 14-d and (b) 360-d samples after subtraction of the Si contribution as described in the text. Solid line = experimental data; dotted line = least-squares fit.

the EXAFS sensitivity to be increased. Furthermore it proves the consistency of the overall spectral fit strategy.

6. DISCUSSION

6.1. Ni Environment

In this study the uptake of Ni on montmorillonite was investigated by P-EXAFS measurements with highly oriented self-supporting Ni-treated montmorillonite films. The P-EXAFS data show a pronounced angular dependence that allows in-plane and out-of-plane contributions in the P-EXAFS spectra to be distinguished. In a previous P-EXAFS and powder EXAFS study on Ni uptake onto the same montmorillonite material at higher pH and Ni concentration (pH 8, $[Ni]_{initial}$ = 660 μM, 0.3 mol/L $NaClO_4$), the formation of a neoformed Ni-phyllosilicate phase was observed (Dähn et al., 2002b). This earlier study indicated that the neoformed Ni-phyllosilicate phase was already present after a short reaction time (1 d), suggesting that Ni nucleation in clay systems can occur quickly. Although the study allowed the identification of a neoformed Ni phase, the binding of Ni to surface sites of montmorillonite could not be investigated. The observation of the latter was prevented because of the strong backscattering contribution of Ni-Ni pairs compared with Ni-Al pairs at distances from 3.0 to 3.1 Å. Therefore, in the present study, Ni uptake on montmorillonite was investigated at a lower pH (7.2) and a lower Ni concentration ($[Ni]_{initial}$ = 19.9 μM; see section 4.2). Even though the Ni loadings were as low as 4 μmol/g (250 ppm sorbed Ni), good-quality P-EXAFS data could be obtained (Fig. 4). Data analysis confirmed the absence of Ni-Ni pairs in all of the P-EXAFS spectra, even after the longest reaction time of 360 d. This finding enabled the binding of Ni atoms to surface sites of montmorillonite to be investigated.

The P-EXAFS study indicates the presence of one Ni-Al and two Ni-Si pairs. The angular variations of $CN^{exafs}_{Ni\text{-}Al}$, $CN^{exafs}_{Ni\text{-}Si1}$, and $CN^{exafs}_{Ni\text{-}Si2}$ observed in structural data of the Ni-treated

Table 5. Structural information derived from P-EXAFS analysis for Al at α = 10°.

	Ni-O			Ni-Al				
Days	$CN^{exafs}_{Ni\text{-}O}$	$R_{Ni\text{-}O}$ (Å)	σ^2 (Å^2)	$CN^{exafs}_{Ni\text{-}Al}$	$R_{Ni\text{-}Al}$ (Å)	σ^2 (Å^2)	ΔE_0 (eV)	%Res
360	5.1	2.03	0.005	2.3	2.99	0.005	−0.8	5.0
14	5.3	2.03	0.005	1.5	3.01	0.005[a]	−0.8	4.9
14	5.3	2.03	0.005	2.2	3.01	0.01	−0.2	4.8

[a] Fixed to the value determined for the 360-day sample.

montmorillonite films (Tables 2 and 3) indicate that the Ni-Al and the two Ni-Si pairs have the same orientations as Al-Al and Al-Si pairs in the montmorillonite platelets. The experimentally determined β^{real} angles ($\beta^{real}_{Ni\text{-}Al} = 90°$, $\beta^{real}_{Ni\text{-}Si1} = 32°$ to 38°, and $\beta^{real}_{Ni\text{-}Si2} = 42°$ to 44°, Table 4) are similar to the β angles in the montmorillonite structure ($\beta^{cryst}_{Al\text{-}Al} = 90°$, $\beta^{cryst}_{Al\text{-}Si1} \sim 33°$ and $\beta^{cryst}_{Al\text{-}Si2} \sim 35°$).

The results presented in Tables 2 and 3 suggest that the Ni-Al and Ni-Si bond distances determined from data analysis ($R_{Ni\text{-}Al} = 2.99$ to 3.01 Å, $R_{Ni\text{-}Si1} = 3.10$ to 3.12 Å, $R_{Ni\text{-}Si2} =$ 3.26 to 3.27 Å) are close to the Al-Al and Al-Si bond distances in montmorillonite (Table 1; Tsipursky and Drits, 1984). Furthermore, the EXAFS study revealed the presence of a Ni-Si2 pair at a distance of 3.26 Å, which is characteristic for tetrahedral Ni-Si linkages in Ni-bearing clays (Manceau and Calas, 1986; Charlet and Manceau, 1994; Dähn et al., 2002b).

The above findings support the hypothesis that Ni is structurally linked to the montmorillonite lattice, and we propose that Ni is either bonded to the clay material as a surface complex or is incorporated into the montmorillonite structure. These two possibilities will be discussed in the following sections in more detail.

6.2. Structural Relationship between Ni and Montmorillonite

6.2.1. Diffusion of Ni into the Montmorillonite Structure

The diffusion of Ni into montmorillonite was investigated by Muller et al. (1997) by saturating montmorillonite with Ni cations and heating the clay material up to 350°C (Hoffman and Klemen, 1950) before EXAFS and X-ray diffraction measurements. Data analysis indicated ~2 Ni-Fe and ~4 Ni-Al/Mg pairs at ~3.02 Å and ~4 Ni-Si pairs at ~3.25 Å. The structural data were interpreted as spectroscopic evidence for the diffusion of Ni into the cv sites of montmorillonite. One might now speculate that although we worked at room temperature, a similar process occurred in our sorption system over the timescale of 1 yr.

To evaluate whether the diffusion of Ni into montmorillonite is a possible uptake mode, we have simulated the diffusion of Ni into a cv position (Ni1 in Fig. 12a). Diffusion into tv sites can be excluded on the basis of the arguments given in section 1. Assuming Ni diffuses into cv sites one would expect $CN^{exafs}_{Ni\text{-}Al,\alpha}$ to increase with time and the X-ray absorber would be surrounded by 6 Al at ~3.0 Å and 4 Si2 at ~3.23 Å (Table 1). Indeed, the data shown in Tables 2 and 3 suggest that the number of neighboring Al atoms slightly increases (from 1.6 to 2.0 at 3.0 Å) with reaction time. The data analysis further suggests that Ni is surrounded ~4 Si at 3.26 to 3.27 Å (Tables 2 and 3). Although the Ni-Si2 structural parameters agree well, there is a serious discrepancy in the $CN^{exafs}_{Ni\text{-}Al,\alpha=35°}$ value ($\leq$2 instead of 6). Thus, it appears that the diffusion of Ni into cv sites occurs, if at all, only to a small amount (<10%). Furthermore, the data can be fitted equally well when the system disorder was allowed to vary (see section 5.3 and Table 5). In that case, the Ni-Al coordination numbers remained unchanged with increasing reaction time (see section 5.3 and Table 5).

One might argue that $CN^{exafs}_{Ni\text{-}Al,\alpha=35°}$ is lowered as a result of destructive interferences with substituting atoms in the octahedral sheet (Mg, Fe). Although Al and Mg have a similar backscattering amplitude and phase shift at the Ni K-edge, the Ni-Al pairs are indeed out of phase with Ni-Fe pairs. Because the Fe content in the STx-1 montmorillonite material is low (17 wt% Al + Mg, <1 wt% Fe; corresponding to an atomic ratio of 1 (Al + Mg): 0.03 (Fe); see section 4.1), it is unlikely that the $CN^{exafs}_{Ni\text{-}Al,\alpha=35°}$ value is significantly modified because of Ni-Fe pairs.

Thus, on the basis of the arguments in this section, it appears unlikely that diffusion of Ni atom into the montmorillonite structure is the major process responsible for the data measured in this study.

6.2.2. Sorption of Ni to Montmorillonite Edge Sites

EXAFS data analysis indicates $CN^{cryst}_{Ni\text{-}Al} \sim 2 \pm 0.5$, $CN^{cryst}_{Ni\text{-}Si1} \sim 2 \pm 0.5$ and $CN^{cryst}_{Ni\text{-}Si2} \sim 4 \pm 0.5$ (see Tables 2 and 3). In the following, we discuss the extent to which Ni surface complexes located at the edges of montmorillonite can explain the EXAFS results presented in this study. Figure 12 illustrates examples of possible Ni surface complexes at the edges of montmorillonite. For the purpose of visualization, the surface complexes are shown separately for sorption onto cv and tv edge sites (Figs. 12a ,b, respectively). The figure illustrates two possible surface complexes formed at cv edge sites (Fig. 12a, Ni2: bonded to two Al atoms at $R_{Ni\text{-}Al}$ ~3.0 Å and two Si2 atoms at $R_{Ni\text{-}Si2}$ ~3.23 Å; Ni3: bonded to three Al atoms and four Si2) and at tv edge sites (Fig. 12b, Ni4: bonded to two Al atoms at $R_{Ni\text{-}Al}$ ~3.0 Å and four Si1 at $R_{Ni\text{-}Si1} = 3.16$ to 3.18 Å; Ni5: bonded to three Al atoms and two Si1).

Although $CN^{cryst}_{Ni\text{-}Al} \sim 2$ is in accordance with the sorption of Ni onto cv- and to tv-like edge sites, it does not allow to speculate whether sorption onto cv- or tv-like edge sites is the dominant uptake mode. A similar conclusion can be made for the neighboring Si atoms. It is clear from the proposed surface complexes above that neither sorption to tv- or cv-like edge sites alone can account for the coordination numbers ($CN^{cryst}_{Ni\text{-}Si1} < 2$ and $CN^{cryst}_{Ni\text{-}Si2} \sim 4$). Thus, we propose that Ni is sorbed onto montmorillonite as a mixture of surface complexes bond to cv- and tv-like edge sites.

Schlegel et al. (1999) observed the presence of inner-sphere surface complexes in an investigation on the uptake of Co on hectorite (a magnesian trioctahedral clay) at pH 6.5 (0.3 $NaNO_3$, solid/liquid 1.95 gL^{-1}, $[Co]_{initial} = 100$ μM, Co sorbed 37 μmol/g). Data analysis revealed the presence of two nearest cationic subshells containing 1.6 ± 0.5 Mg at 3.03 Å and 2.2 ± 0.5 Si at 3.27 Å. The angular dependence indicated that Co-Mg pairs are oriented parallel to the film plane, whereas the Co-Si pairs are not. The results were interpreted in terms of the formation of Co inner-sphere mononuclear surface complexes located at the edges of hectorite platelets in the continuity of the octahedral sheet. The findings of this study are comparable to those of Schlegel et al. (1999) and demonstrate that heavy metals binding to edge sites is not only a sorption mechanism for trioctahedral smectites but also for dioctahedral smectites. It should be noted that our study indicates the presence of two Si distances, whereas Schlegel et al. (1999) observed only one characteristic Ni-Si pair. This fact is consistent with the structural differences between di- and trioctahedral clays (see section 1).

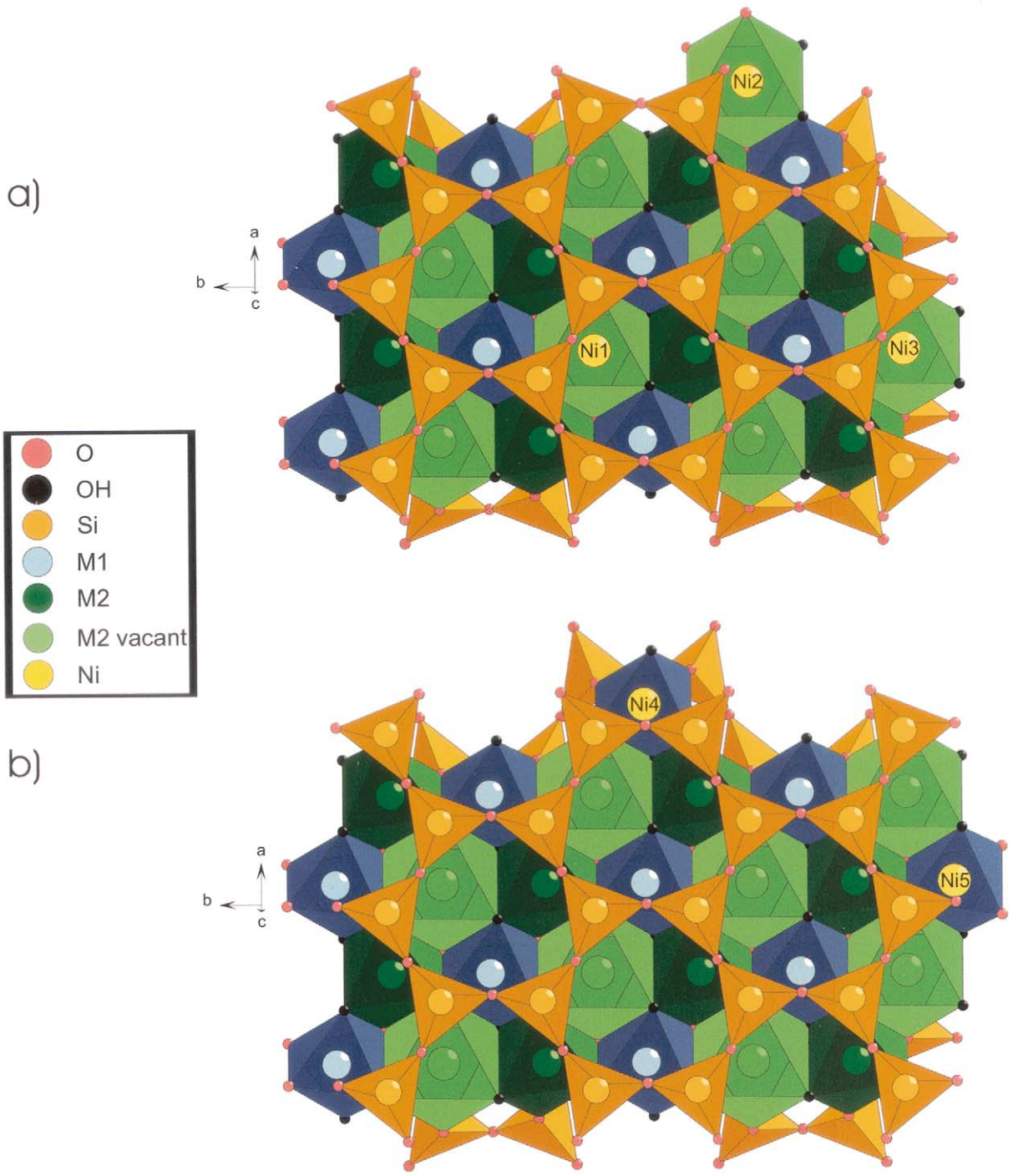

Fig. 12. Simulations of possible positions of Ni incorporated in the octahedral sheet and sorbed to the *ab* plane of montmorillonite for (a) cv and (b) tv sites.

6.3. Effect of Surface Loading and Reaction Conditions on Ni Surface Complexes on Montmorillonite

The number of edge sites can be estimated from morphologic information. In a previous study we calculated relative surface areas for montmorillonite (2% for edge surfaces [(100), (110), and (010)] and 98% for the (001) surface; Dähn et al., 2002a). Because sorption to planar sites is blocked as a result of the high ionic strength of the solution (0.3 mol/L $NaClO_4$), only lateral surfaces are considered. On the basis of the density of oxygen atoms at the montmorillonite lateral surfaces, it is then possible to estimate the number of edge sites (Tsipursky and Drits, 1984). This approach yields 0.5 sites/nm^2 for the lateral surfaces (excluding the (001) surface). This number is the same

order as the number of amphoteric edge sites for montmorillonite deduced by potentiometric titration (1.4 sites/nm^2; Baeyens and Bradbury, 1995a). Estimated site densities obtained from different methods typically differ by factors of at least 2 to 3 (Keren and Sparks, 1995). Finally, we assumed that Ni is bonded to two Al atoms from the montmorillonite structure (Tables 2, 3, and 5), thus reducing the number of lateral sites from 0.5 to 0.25 sites/nm^2. Accordingly, the Ni-treated montmorillonite samples (4 and 7 μmol/g) are clearly below a monolayer coverage (surface coverage: 11 and 19%). This finding can explain the absence of Ni-Ni pairs in the P-EXAFS data. Furthermore, it is justifiable to propose that although the Ni loading increased over time, the increase in Ni surface coverage had no major effect on the uptake mode and that as suggested by the P-EXAFS data, the predominant uptake mode is determined by the same complexes formed in both samples.

7. CONCLUDING REMARKS

The present study showed that the amount of Ni sorbed onto the montmorillonite slowly increased over the course of 1 yr. Similar slow sorption phenomena have been reported in the literature (e.g., Nelson and Melsted, 1955; Gadde and Laitinen, 1974; Kuo and Mikkelsen, 1980; McKenzie, 1980; Brümmer et al., 1988; Barrow, 1989; McBride, 1994). It has been speculated that slow metal uptake processes are caused by slow sorption or diffusion processes, by the formation of new phases with time, or both. Spectroscopic evidence for the latter mechanism was found in several recent studies at elevated metal concentration (Scheidegger et al., 1998; Thompson et al., 1999; Schlegel et al., 2001a; Dähn et al., 2002b). This study shows that the diffusion of Ni atoms into the montmorillonite structure is not the dominant uptake mode and that the formation of new Ni nucleation products with time can be excluded. We have found spectroscopic evidence for the formation of surface complexes on the edge sites of montmorillonite. Data analysis revealed that these surface complexes either become more ordered with time or that the Ni-Al coordination numbers are slightly increasing with increasing reaction time.

We can speculate that these findings can explain some observations made in desorption experiments carried out in our laboratory. Experiments at trace element concentration indicated that the release of Ni sorbed onto montmorillonite became increasingly hindered with prolonged sorption times. Similar “hysteresis phenomena” have been observed for example investigating the desorption behavior of Ca, Cr, Co, Ni, Cu, and Zn sorbed onto ferrihydrite (Schultz et al., 1987; Ainsworth et al., 1994) and Co and Cd sorbed onto Fe and Mn oxides (Backes et al., 1995). Like most of the research on the uptake of heavy metals on clay minerals, the above studies were based on a macroscopic approach. The present study combined macroscopic and P-EXAFS investigations and thus highlights the necessity of following uptake mechanisms of heavy metals on clay mineral surfaces over extended reaction times (months to years) with spectroscopic methods.

The findings presented in this study are of significant environmental relevance because montmorillonite is overwhelmingly abundant in the environment. On the basis of the similarities between this study and the study of Schlegel et al. (1999) (sorption of Co onto edge sites of hectorite), we speculate that the findings determined by P-EXAFS can also be extrapolated to other di- and trioctahedral clays.

Finally, because the attachment of metal ions specifically bond to clay mineral surfaces can severely reduce their bioavailability and mobility in soil and water environments, molecular-level information is crucial for improving mechanistic models on the long-term fate of heavy metal in the geosphere. The findings presented in this study are an important step toward a molecular-level description of metal uptake onto clay minerals and will help to improve our understanding of metal sorption processes at the water–mineral interface.

Acknowledgments—We thank Pierre-Emmanuel Petit (European Synchrotron Radiation Facility [ESRF], Grenoble, France) for his support during the XAFS measurements and the European Synchrotron Radiation Facility (ESRF) at Grenoble, France, for the provision of beam time. We thank Enzo Curti for the determination of the structural formula of the STx-1. Partial financial support was provided by the National Cooperative for the Disposal of Radioactive Waste (Nagra), Wettingen, Switzerland. The handling of the manuscript by Samuel J. Traina and the constructive and helpful comments of two anonymous reviewers are gratefully acknowledged.

Associate editor: S. J. Traina

REFERENCES

Ainsworth C. C., Pilon J. L., Gassman P. L., and Van Der Sluys W. G. (1994) Cobalt, cadmium, and lead sorption to hydrous iron oxide: Residence time effect. *Soil Sci. Soc. Am. J.* **58,** 1615–1623.

Backes C. A., McLaren R. G., Rage A. W., and Swift R. S. (1995) Kinetics of cadmium and cobalt desorption from iron and manganese oxides. *Soil Sci. Soc. Am. J.* **59,** 778–785.

Baes C. F. and Mesmer R. E. (1976) *The Hydrolysis of Cations*. Wiley.

Baeyens B., and Bradbury M. H. (1995a) A quantitative mechanistic description of Ni, Zn and Ca sorption on Na-montmorillonite. Part I: Physico-chemical characterisation and titration measurements. PSI Bericht No. 95-10. Paul Scherrer Institut, Villigen, Switzerland, and Nagra Technical Report NTB95-04, Nagra, Wettingen, Switzerland.

Baeyens B., and Bradbury M. H. (1995b) A quantitative mechanistic description of Ni, Zn and Ca sorption on Na-montmorillonite. Part II: Sorption measurements. PSI Bericht No. 95-11. Paul Scherrer Institut, Villigen, Switzerland, and Nagra Technical Report NTB95-05, Nagra, Wettingen, Switzerland.

Baeyens B. and Bradbury M. H. (1997) A mechanistic description of Ni and Zn sorption on Na-montmorillonite. Part I: Titration and sorption measurements. *J. Contam. Hydrol.* **27,** 199–222.

Barrow N. J. (1989) Reaction kinetics of the adsorption and desorption of nickel, zinc, and cadmium by goethite: II Modelling the extent and rate of reaction. *Soil Sci. Soc. Am. J.* **40,** 437–450.

Bradbury M. H. and Baeyens B. (1997) A mechanistic description of Ni and Zn sorption on Na-montmorillonite. Part II: Modelling. *J. Contam. Hydrol.* **27,** 223–248.

Britton H. T. S. (1925) Electrometric studies of the precipitation of hydroxides. Part IV. Precipitation of mercury, cadmium, lead, silver, cupric, uranic, and ferric hydroxides by use of the oxygen electrode. *J. Chem. Soc.* **127,** 2148–2159.

Brümmer G. W., Gerth J., and Tiller K. G. (1988) Reaction kinetics of the adsorption and desorption of nickel, zinc and cadmium by goethite. I. Adsorption and diffusion of metals. *J. Soil Sci.* **39,** 37–52.

Bunge H. J. and Esling C., eds. (1982) *Quantitative Texture Analysis.* Deutsche Gesellschaft für Metallkunde.

Castañer R. and Prieto C. (1997) Fluorescence detection of extended X-ray absorption fine structure in thin films. *J. Phys. III France* **7,** 337–349.

Charlet L. and Manceau A. (1994) Evidence for the neoformation of clays upon sorption of Co(II) and Ni(II) on silicates. *Geochim. Cosmochim. Acta* **58,** 2577–2582.

Dähn R., Scheidegger A. M., Manceau A., Schlegel M. L., Baeyens B., and Bradbury M. H. (2001) Ni clay neoformation on montmorillonite surface. *J. Synchr. Rad.* **8,** 533–535.

Dähn R., Scheidegger A. M., Manceau A., Curti E., Baeyens B., Bradbury M. H., and Chateigner D. (2002a) Th uptake on montmorillonite: A powder and polarized extended X-ray absorption fine structure (EXAFS) study. *J. Colloid Interface Sci.* **249,** 8–21.

Dähn R., Scheidegger A. M., Manceau A., Schlegel M. L., Baeyens B., Bradbury M. H., and Morales M. (2002b) Neoformation of Ni phyllosilicate upon Ni uptake on montmorillonite: A kinetics study by powder and polarized EXAFS. *Geochim. Cosmochim. Acta* **66**(13), 2335–2347.

Dittmer J. and Dau H. (1998) Theory of the linear dichroism in the extended X-ray absorption fine structure (EXAFS) of partially vectorially ordered systems. *J. Phys. Chem. B* **102,** 8196–8200.

Furrer G., Zysset M., and Schindler P. W. (1993) Weathering kinetics of montmorillonite: Investigations in batch and mixed-flow reactors. In *Geochemistry of Clay–Pore Fluid Interactions*, Vol. 4 (eds. D. A. C. Manning, P. L. Hall, and C. R. Hughes), pp. 243–262. Chapman & Hall.

Gadde R. R. and Laitinen H. A. (1974) Studies of heavy metal adsorption by hydrous iron and manganese oxides. *Anal. Chem.* **46,** 2022–2026.

Gauthier C., Goulon J., Moguiline E., Rogalev A., Lechner P., Struder L., Fiorini C., Longoni A., Sampietro M., Besch H., Pfitzner R., Schenk H., Tafelmeier U., Walenta A., Misiakos K., Kavadias S., and Loukas D. (1996) A high resolution, 6 channel, silicon drift detector array with integrated JFET's designed for XAFS spectroscopy: First X-ray fluorescence excitation spectra recorded at the ESRF. *Nucl. Instrum. Meth. Phys. Res.* **A382,** 524–532.

Gauthier C., Solé V. A., Signorato R., Goulon J., and Moguiline E. (1999) The ESRF beamline ID26: X-ray absorption on ultra dilute sample. *J. Synchr. Rad.* **6,** 164–166.

Güven N. (1988) Smectites. In *Hydrous Phyllosilicates (Exclusive Micas)*, Vol. 19 (ed. S. W. Bailey), pp. 497–559. Mineralogical Society of America.

Heydemann A. (1966) Über die chemische Verwitterung von Tonmineralen (Experimentelle Untersuchungen). *Geochim. Cosmochim. Acta* **30,** 995–1035.

Hoffman V. and Klemen R. (1950) Loss on heating of the ability of lithium ions to exchange in bentonite. *Z. Anorg. Allgem. Chem.* **262,** 95–99.

Keren R. and Sparks D. L. (1995) The role of edge surfaces in flocculation of 2:1 clay minerals. *Soil Sci. Soc. Am. J.* **59,** 430–435.

Kuo R. J. and Mikkelsen D. S. (1980) Kinetics of zinc desorption from soils. *Plant Soil.* **56,** 355–364.

Manceau A. (1990) Distribution of cations among the octahedra of phyllosilicates: Insight from EXAFS. *Can. Mineral.* **28,** 321–328.

Manceau A. and Calas G. (1986) Nickel-bearing clay minerals: II. Intracrystalline distribution of nickel: An X-ray absorption study. *Clay Minerals* **21,** 341–360.

Manceau A., Bonnin D., Kaiser P., and Fretigny C. (1988) Polarized EXAFS of biotite and chlorite. *Phys. Chem. Minerals* **16,** 180–185.

Manceau A., Bonnin D., Stone W. E. E., and Sanz J. (1990) Distribution of Fe in the Octahedral Sheet of Trioctahedral Micas by Polarized EXAFS. *Phys. Chem. Minerals* **17,** 363–370.

Manceau A., Chateigner D., and Gates W. P. (1998) Polarized EXAFS, distance-valence least-squares modeling (DVLS) and quantitive texture analysis approaches to the structural refinement of Garfield nontronite. *Phys. Chem. Minerals* **25,** 347–365.

Manceau A., Schlegel M. L., Chateigner D., Lanson B., Bartoli C., and Gates W. P. (1999) Application of polarized EXAFS to fine-grained layered minerals. In *Synchrotron X-ray Methods in Clay Science* (ed. D. G. Schulze, J. W. Stucki, and P. M. Bertsch), pp. 68–114. The Clay Mineral Society.

Manceau A. and Schlegel M. L. (2001) Texture effect on polarized EXAFS amplitude. *Phys. Chem. Mineral.* **28,** 52–56.

Mattigod S. V., Rai D., Felmy A. R., and Rao L. (1997) Solubility and solubility product of crystalline $Ni(OH)_2$. *J. Solution Chem.* **26,** 391–403.

McBride M. B. (1994) *Environmental Chemistry of Soils.* Oxford University Press.

McKenzie R. M. (1980) The adsorption of lead and other heavy metals on oxides of manganese and iron. *Aust. J. Soil Res.* **18,** 61–73.

Morton J. D., Semrau J. D., and Hayes K. F. (2001) An X-ray absorption spectroscopy study of the structure and reversibility of copper adsorbed to montmorillonite clay. *Geochim. Cosmochim. Acta* **65,** 2709–2722.

Muller F., Besson G., Manceau A., and Drits V. A. (1997) Distribution of isomorphous cations within octahedral sheets in montmorillonite from Camp-Bertaux. *Phys. Chem. Minerals* **24,** 159–166.

Nelson J. L. and Melsted S. W. (1955) The cemistry of zinc added to soils and clays. *Soil Sci. Soc. Am. J.* **19,** 439–443.

O'Day P. A., Parks G. A., and Brown G. E. Jr. (1994) Molecular structure and binding sites of cobalt(II) surface complexes on kaolinite from X-ray absorption spectroscopy. *Clays Clay Minerals* **42,** 337–355.

Pandya K. I., O'Grady W. E., Corrigan D. A., McBreen J., and Hoffman R. W. (1990) Extended X-ray absorption fine structure investigation of nickel hydroxides. *J. Phys. Chem.* **94,** 21–26.

Perdikatsis B. and Burzlaff H. (1981) Strukturverfeinerung am Talk Mg_3 $[(OH)_2Si_4O_{10}]$. *Zeitschr. Kristallogr.* **156,** 177–186.

Plyasunova N. V., Zhang Y., and Muhammed M. (1998) Critical evalution of thermodynamics of complex formation of metal ions in aqueous solutions. IV. Hydrolysis and hydroxo-complexes of Ni^{2+} at 298.15 K. *Hydrometallurgy* **48,** 43–63.

Rehr J. J., Mustre de Leon J., Zabinsky S., and Albers R. C. (1991) Theoretical X-ray absorption fine structure standards. *J. Am. Chem. Soc.* **113,** 5135–5140.

Ressler T. (1998) WinXAS: A program for X-ray absorption spectroscopy data analysis under MS-Windows. *J. Synchr. Rad.* **5,** 118–122.

Scheidegger A. M., Lamble G. M., and Sparks D. L. (1997) Spectroscopic evidence for the formation of mixed-cation hydroxide phases upon metal sorption on clays and aluminum oxides. *J. Colloid Interface Sci.* **186,** 118–128.

Scheidegger A. M., Strawn D. G., Lamble G. M., and Sparks D. L. (1998) The kinetics of mixed Ni-Al hydroxide formation on clay and aluminum oxide minerals: A time-resolved XAFS study. *Geochim. Cosmochim. Acta* **62,** 2233–2245.

Schlegel M. L., Manceau A., Chateigner D., and Charlet L. (1999) Sorption of metal ions on clay minerals: 1. Polarized EXAFS evidence for the adsorption of Co on the edges of hectorite particles. *J. Colloid Interface Sci.* **215,** 140–158.

Schlegel M. L., Manceau A., Charlet L., Chateigner D., and Hazemann J. L. (2001a) Sorption of metal ions an clay minerals. 3. Nucleation and epitaxial growth of Zn phyllosilicate on the edges of hectorite. *Geochim. Cosmochim. Acta* **65,** 4155–4170.

Schlegel M. L., Manceau A., Charlet L., and Hazemann J. L. (2001b) Adsorption mechanisms of Zn on hectorite as a function of time, pH, and ionic strength. *Am. J. Sci.* **301**(9), 798–830.

Schultz M. F., Benjamin M. M., and Ferguson J. F. (1987) Adsorption and desorption of metals on ferrihydrite: Reversibility of the reaction and sorption properties of the regenerated solid. *Environ. Sci. Technol.* **21,** 863–869.

Signorato R. and Solé V. A. (1999) Perfomance of the ESRF ID26 beamline reflective optics. *J. Synchr. Rad.* **6,** 176–177.

Sposito G. (1984) *The Surface Chemistry of Soils*. Oxford University Press, New York.

Stumm W. and Morgan J. J. (1981) *Aquatic Chemistry: An Introduction Emphasizing Chemical Equilibria in Natural Waters.* Wiley.

Teo B. K. (1986) *EXAFS: Basic Principles and Data Analysis.* Springer-Verlag.

Thompson H. A., Parks G. A., and Brown G. E. Jr. (1999) Dynamic interactions of dissolution, surface adsorption, and precipitation in an aging cobalt(II)–clay–water system. *Geochim. Cosmochim. Acta* **63,** 1767–1779.

Tröger L., Zschech E., Arvanitis D., and Baberschke K. (1992) Quantitative fluorescence EXAFS analysis of concentrated samples—Correction of the self-absorption effect. *Jpn. J. Appl. Phys.* **32,** 144–146.

Tsipursky S. I. and Drits V. A. (1984) The distribution of octahedral cations in the 2:1 layers of dioctahedral smectites studied by oblique-texture electron diffraction. *Clay Minerals* **19,** 177–193.

Van Olphen H. and Fripiat J. J. (1979) *Data Handbook for Clay Materials and Other Non-Metallic Minerals.* Pergamon Press.

Westall J. C. and Hohl H. (1980) A comparison of electrostatic models for the oxide/solution interface. *Adv. Coll. Inter. Sci.* **12,** 265–294.